Supplementary Material

Supplementary Figure S1. Overlay of [^{15}N, ^{1}H] TROSY spectra of PARP-1 CAT domain (residues 657-1014) before and after the lyophylisation procedure described in Materials and Methods in the main paper.

Supplementary Figure S2. Initial electron density for ligands**.** Unbiased difference electron density maps from initial stages of crystallographic structure refinement, before incorporation of the ligand in the model. $|F_{obs}-F_{calc}|$ maps contoured at 3 σ are shown as green mesh.

Supplementary Figure S3. Single-cycle kinetic surface plasmon resonance sensorgrams for A) olaparib, B) veliparib and C) talazoparib binding to full length PARP-1. D) Multi-cycle kinetic sensorgram for EB-47 binding to full length PARP-1.

Supplementary Figure S4. Thermal unfolding of WT CAT domain and L713F, L765F and L765A mutants. Fluorescence ratio data are plotted against temperature.

Supplementary Figure S5. Correlation times for overall tumbling (τ_c) for PARP-1 CAT domain and its complexes with veliparib, olaparib, talazoparib and EB-47.

Supplementary Figure S6. Correlation times for overall tumbling (τ_c) for WT PARP-1 CAT domain and its point mutants L713F, L765F and L765A.

Supplementary Figure S7. Steady-state {^{1}H} ^{15}N NOE data for PARP-1 CAT domain and its complexes with veliparib, olaparib, talazoparib and EB-47, showing residues of HD subdomain only.

Supplementary Figure S8. Steady-state {^{1}H} ^{15}N NOE data for WT PARP-1 CAT domain and its point mutants L713F, L765F and L765A, showing residues of HD subdomain only.

Supplementary Figure S9. Steady-state {^{1}H} ^{15}N NOE data for PARP-1 CAT domain and its complexes with veliparib, olaparib, talazoparib and EB-47, showing residues of ART subdomain only.

Supplementary Figure S10. Steady-state {^{1}H} ^{15}N NOE data for WT PARP-1 CAT domain and its point mutants L713F, L765F and L765A, showing residues of ART subdomain only.

Supplementary Figure S11. ^{15}N longitudinal relaxation time (T_1) data for PARP-1 CAT domain and its complexes with veliparib, olaparib, talazoparib and EB-47, showing residues of HD subdomain only.

Supplementary Figure S12. ^{15}N longitudinal relaxation time (T_1) data for WT PARP-1 CAT domain and its point mutants L713F, L765F and L765A, showing residues of HD subdomain only.

Supplementary Figure S13. ^{15}N longitudinal relaxation time (T_1) data for PARP-1 CAT domain and its complexes with veliparib, olaparib, talazoparib and EB-47, showing residues of ART subdomain only.

Supplementary Figure S14. ^{15}N longitudinal relaxation time (T_1) data for WT PARP-1 CAT domain and its point mutants L713F, L765F and L765A, showing residues of ART subdomain only.

Supplementary Figure S15. ^{15}N spin-locked relaxation time ($T_{1\rho}$) data for PARP-1 CAT domain and its complexes with veliparib, olaparib, talazoparib and EB-47, showing residues of HD subdomain only.

Supplementary Figure S16. ^{15}N spin-locked relaxation time ($T_{1\rho}$) data for WT PARP-1 CAT domain and its point mutants L713F, L765F and L765A, showing residues of HD subdomain only.

Supplementary Figure S17. ^{15}N spin-locked relaxation time ($T_{1\rho}$) data for PARP-1 CAT domain and its complexes with veliparib, olaparib, talazoparib and EB-47, showing residues of ART subdomain only.

Supplementary Figure S18. ^{15}N spin-locked relaxation time ($T_{1\rho}$) data for A) WT PARP-1 CAT domain and its point mutants B) L713F, C) L765F and D) L765A, showing residues of ART subdomain only.

Supplementary Figure S19. Relationship between NH solvent exchange rates and conformational fluctuation rates.

Supplementary Figure S20. Schematic [^{15}N,^{1}H] correlation plots showing chemical shift differences for the amide group ^{1}H and ^{15}N signals of residues in helix F.

Supplementary Figure S21. CD spectra of PARP-1 CAT domain, its complexes with veliparib, olaparib, talazoparib and EB-47, and the point mutants L713F, L765F and L765A.

Supplementary Figure S22. Single-cycle kinetic surface plasmon resonance sensorgrams for A) PARP-1 alone, B) PARP-1 + olaparib, C) PARP-1 + veliparib and D) PARP-1 + EB-47 binding to DNA. Data was fitted to steady state for A)-C). A 1:1 binding kinetic model was used for D).

Supplementary Figure S23. Superpositions of PARP-1 CAT domain in the apo-protein and in inhibitor complexes with veliparib, olaparib, talazoparib and EB-47, in each case superposing each structure onto atoms of 7AAA.

Supplementary Figure S24. Co-ordinate deviations between the different protein chains in the asymmetric unit for the structures of free PARP-1 CAT domain and its complexes with talazoparib, veliparib, olaparib, and EB-47, as well as for chains C and F of the complex of PARP-1 F1, F3 and WGR-CAT with a DNA duplex.

Supplementary Figure S25. B factors for each chain in each of the structures of free PARP-1 CAT domain and its complexes with veliparib, olaparib, talazoparib, and EB-47, as well as for chains C and F of the complex of PARP-1 F1, F3 and WGR-CAT with a DNA duplex.

Supplementary Table S1. Superposition statistics for individual helices of PARP-1 CAT domain (all chains fitted onto 7AAA).

Supplementary Table S2. Superposition statistics for groups of helices in PARP-1 HD subdomain, demonstrating differences in helical packing (all chains fitted onto 7AAA).

Supplementary Table S3. Superposition statistics for individual helices in PARP-1 HD subdomain, comparing different chains in the same structure.

Supplementary Table S4. Superposition statistics for the HD and ART subdomains of PARP-1 CAT domain (all chains onto 7AAA).

Supplementary Table S5. Superposition statistics for the HD and ART subdomains of PARP-1 CAT domain between different complexes with the same inhibitor (all chains).

Supplementary Table S6. Binding affinities and dissociation rate constants for PARP inhibitors as determined in this work and in the literature.

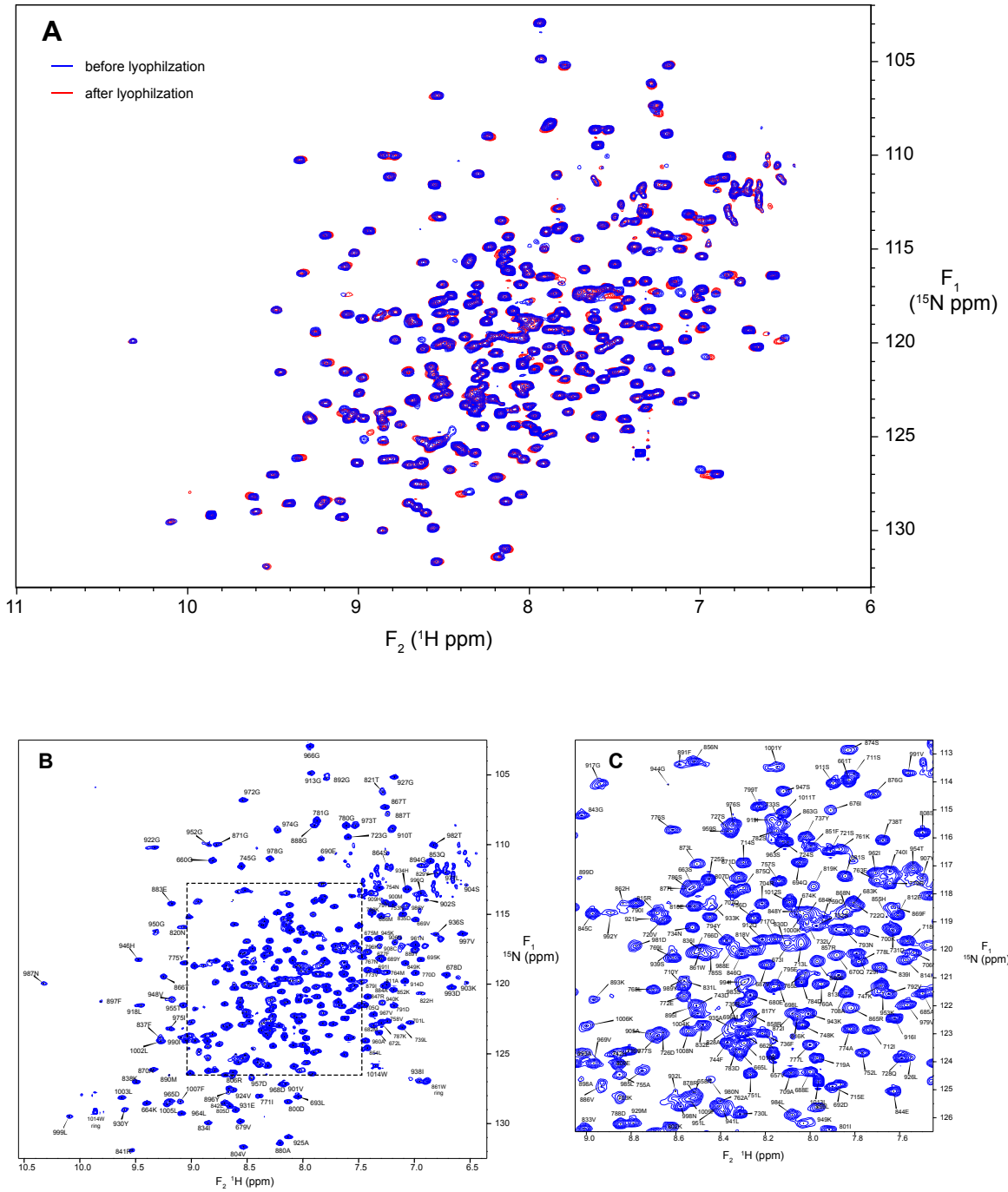

Supplementary Figure S1. A) Overlay of [^{15}N, ^{1}H] TROSY spectra of ^{15}N-labelled PARP-1 CAT domain (residues 656-1014) before (blue) and after (red) the lyophylisation procedure described in Materials and Methods in the main paper; data recorded at 25°C and 800 MHz. For this control the protein was resuspended in H_2O, but in the real-time $^{2}H_2O$ exchange experiments described in the main paper, protein was resuspended in $^{2}H_2O$ and a time series of TROSY spectra recorded. A small number of small differences in chemical shift are likely caused by partial sublimation of buffer components during lyophilsation and did not interfere with interpretation of the data. B) [^{15}N, ^{1}H]-TROSY spectrum of ^{15}N-labelled human PARP-1 CAT domain acquired at 800 MHz and 25 °C, showing backbone amide NH signal assignments. Protein concentration was 400 µM in 50 mM [$^{2}H_{11}$]Tris, pH 7.0, 50 mM NaCl and 2 mM [$^{2}H_{10}$]DTT in 95:5 H_2O/$^{2}H_2O$. C) Expansion of the most heavily overlapped region of the spectrum shown in B).

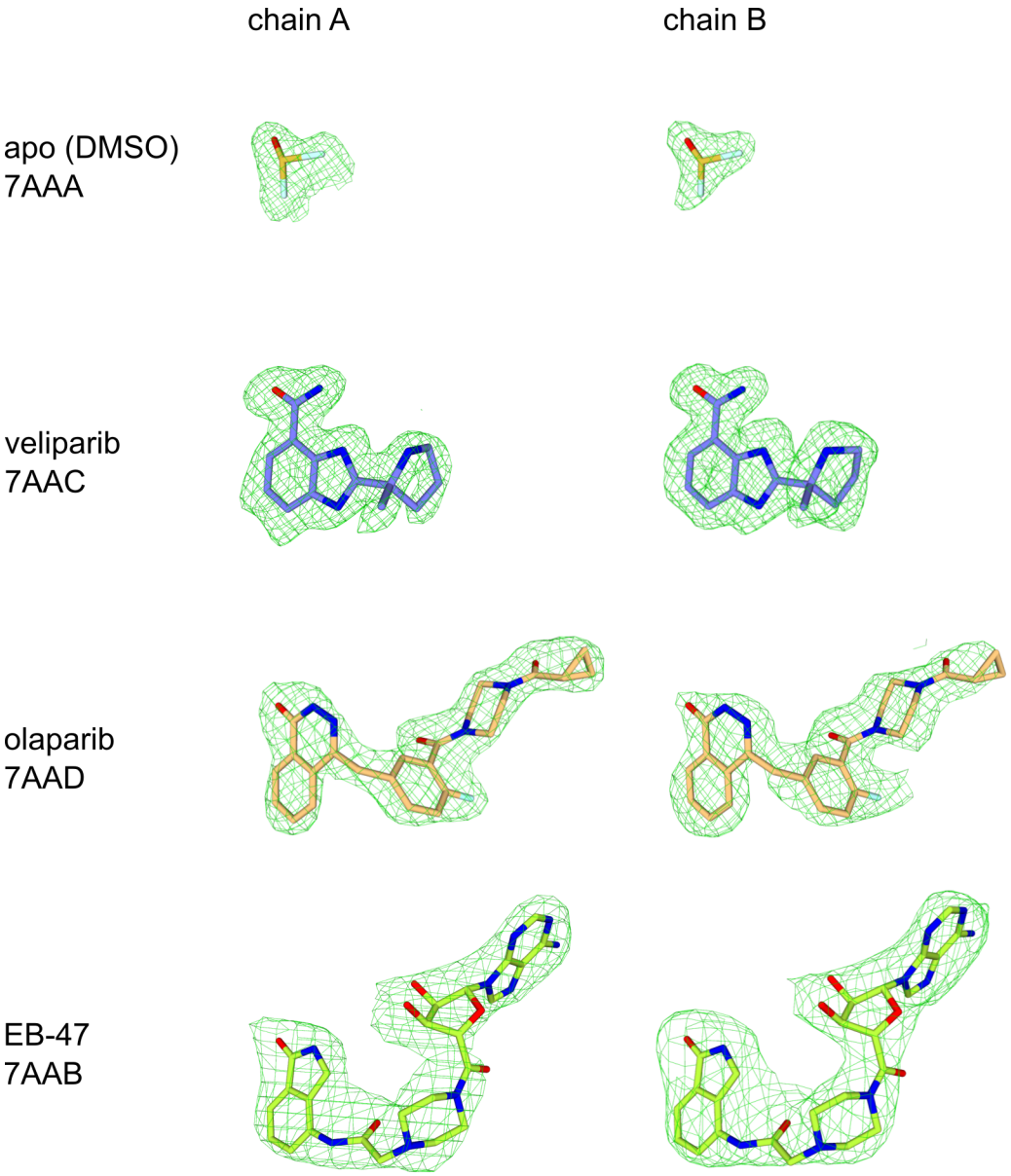

Supplementary Figure S2. Initial electron density for ligands**.** Unbiased difference electron density maps from initial stages of crystallographic structure refinement, before incorporation of the ligand in the model. $|F_{obs}-F_{calc}|$ maps contoured at 3 σ are shown as green mesh.

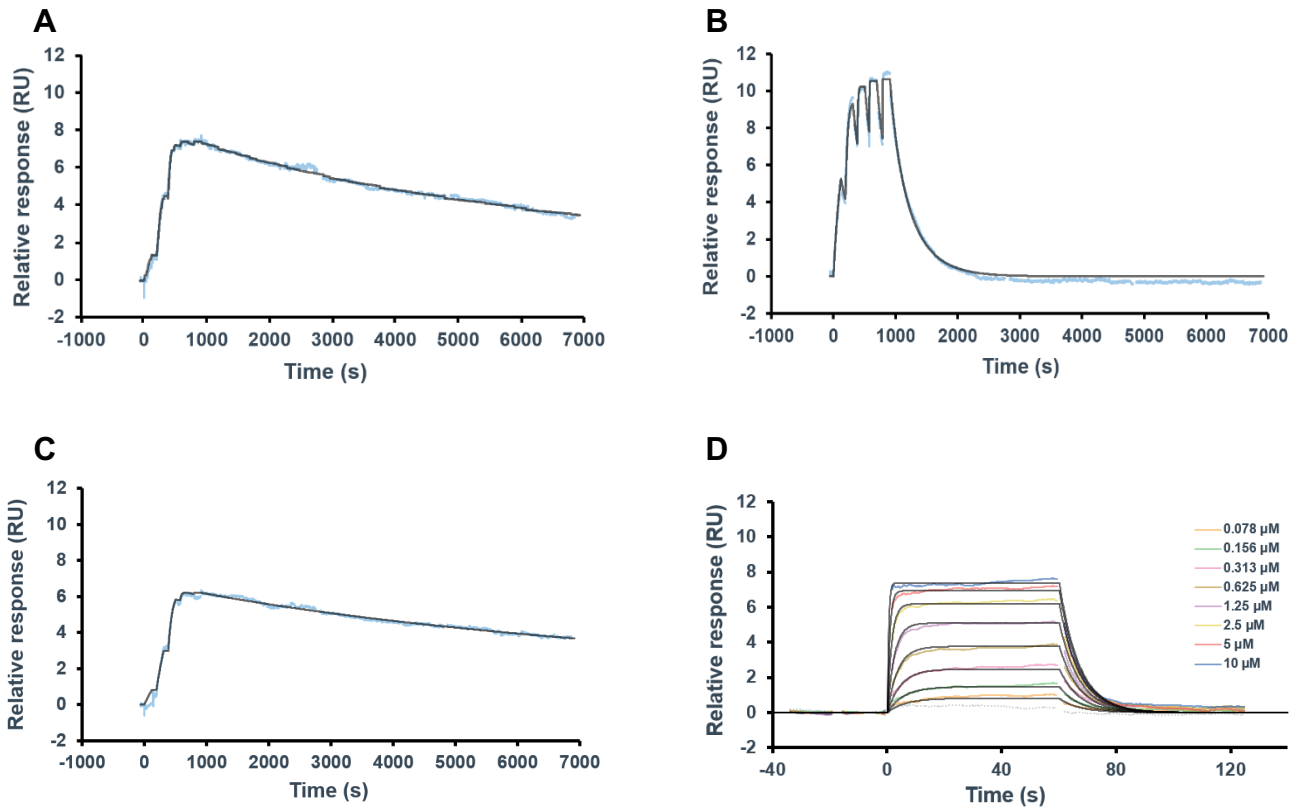

Supplementary Figure S3. Single-cycle kinetic surface plasmon resonance sensorgrams for A) olaparib, B) veliparib and C) talazoparib binding to full length PARP-1. Concentrations used for single cycle kinetics were 0.01, 0.0316, 0.1, 0.316 and 1 µM. D) Multi-cycle kinetic sensorgram for EB-47 binding to full length PARP-1. Light blue/coloured lines are the SPR data, black lines are the fit to a 1:1 binding model. All sensorgrams are representative of at least three separate experiments.

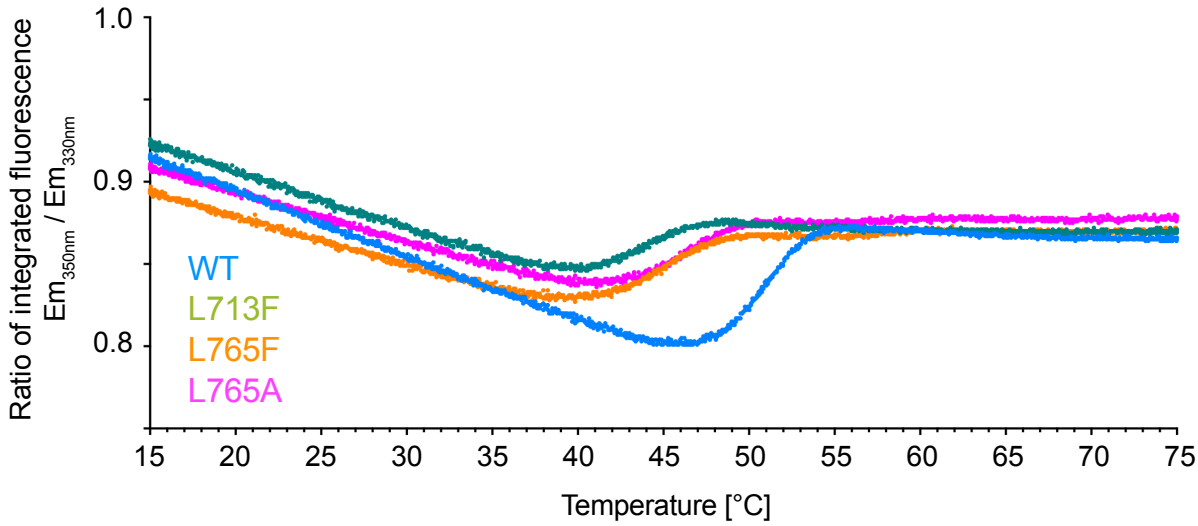

Supplementary Figure S4. Thermal unfolding of WT CAT domain and L713F, L765F and L765A mutants. Fluorescence ratio data are plotted against temperature (all samples contained 500 μM protein in 50 mM Tris buffer, 50 mM NaCl and 2 mM DTT at pH 7.0). The fitted first derivative plots of these data appear in Figure 1K.

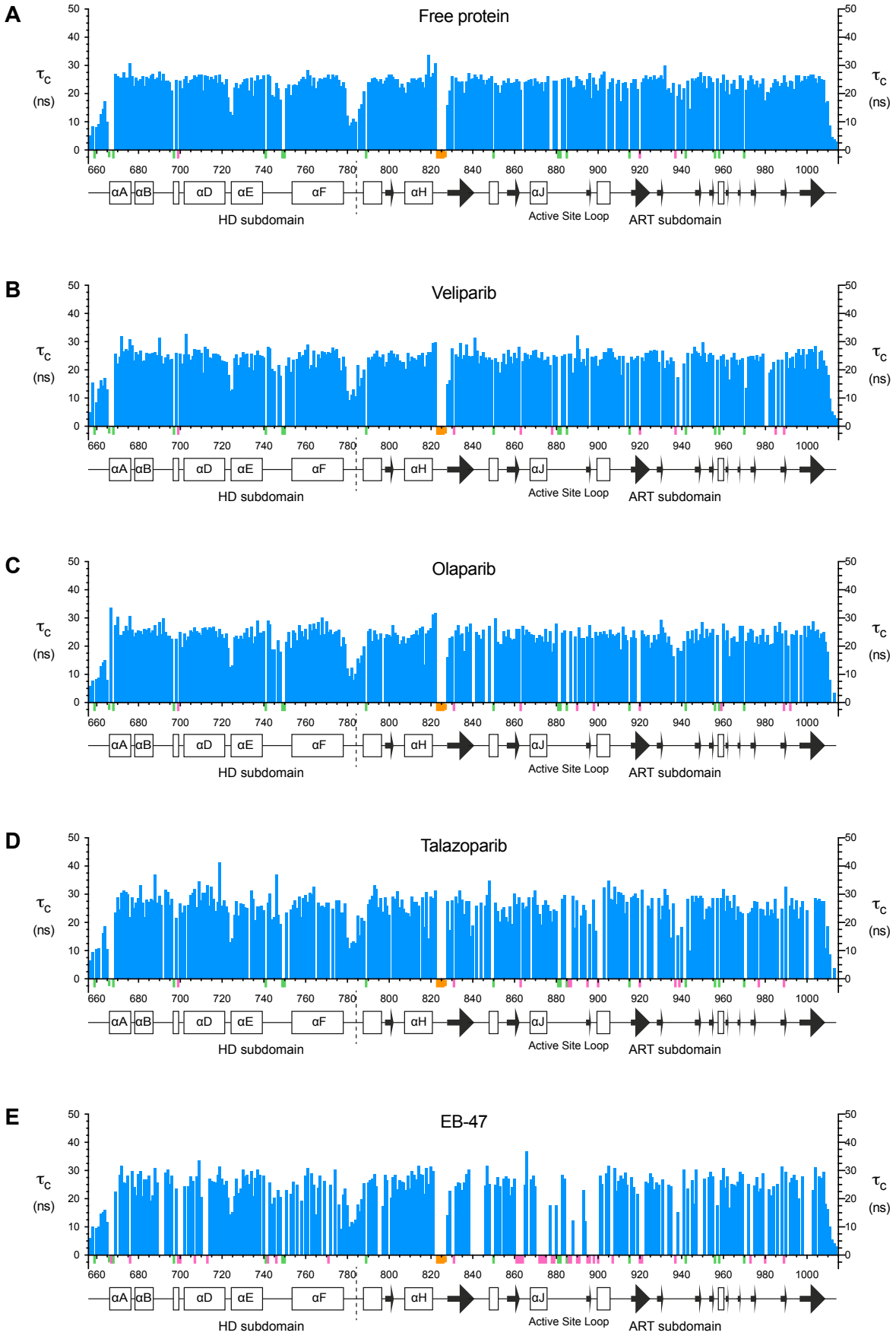

Supplementary Figure S5. Correlation times for overall tumbling (τ_c) for A) PARP-1 CAT domain and its complexes with B) veliparib, C) olaparib, D) talazoparib and E) EB-47. Values were calculated for each residue from T_1 and $T_{1\rho}$ data recorded at 25°C and 800 MHz as described in Materials and Methods. Small coloured bars beneath the sequence scale are used to indicate the positions of prolines (pale green), overlapped or unassigned signals (pink) and the Ala823-Asn827 loop for which no signals were seen in any spectrum (orange).

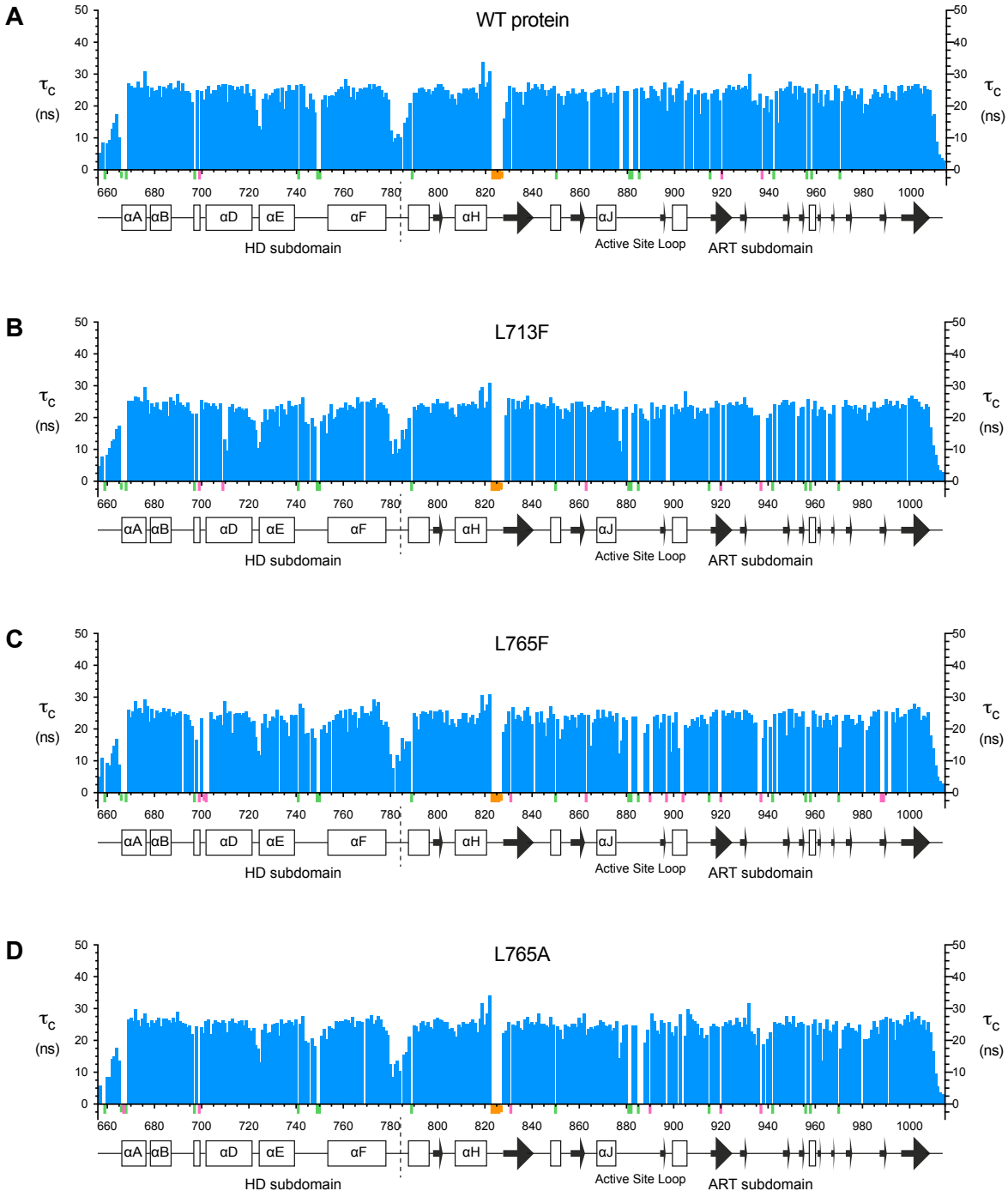

Supplementary Figure S6. Correlation times for overall tumbling (τ_c) for A) WT PARP-1 CAT domain and its point mutants B) L713F, C) L765F and D) L765A. Values were calculated for each residue from T_1 and $T_{1\rho}$ data recorded at 25°C and 800 MHz as described in Materials and Methods. Small coloured bars beneath the sequence scale are used to indicate the positions of prolines (pale green), overlapped or unassigned signals (pink) and the Ala823-Asn827 loop for which no signals were seen in any spectrum (orange).

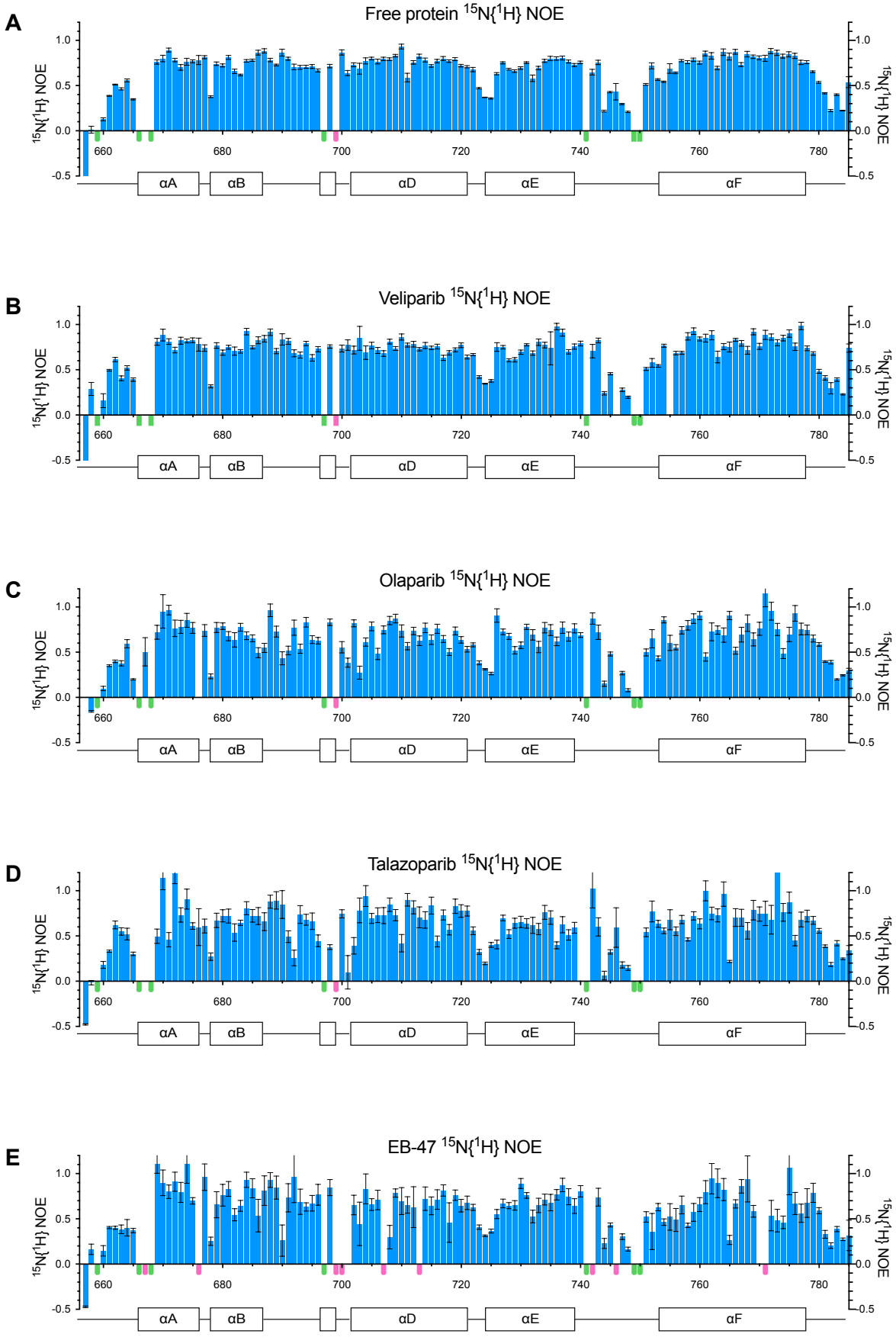

Supplementary Figure S7. Steady-state $\{^{1}H\}$ ^{15}N NOE data recorded at 25°C and 800 MHz for A) PARP-1 CAT domain and its complexes with B) veliparib, C) olaparib, D) talazoparib and E) EB-47, showing residues of HD subdomain only. Small coloured bars beneath the sequence scale are used to indicate the positions of prolines (pale green) and overlapped or unassigned signals (pink). Error bars were derived as described in Materials and Methods.

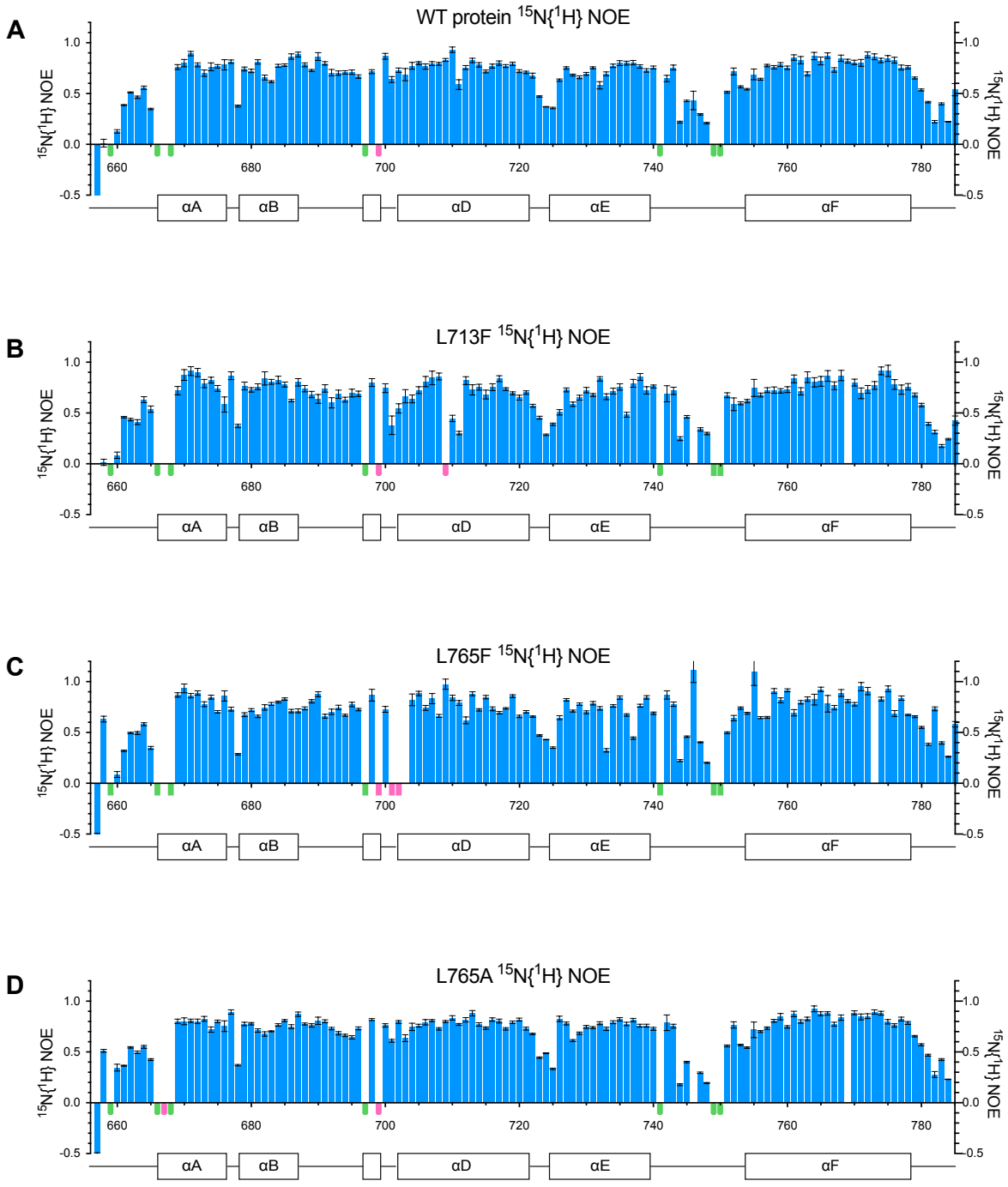

Supplementary Figure S8. Steady-state $\{^{1}H\}$ ^{15}N NOE data recorded at 25°C and 800 MHz for A) WT PARP-1 CAT domain and its point mutants B) L713F, C) L765F and D) L765A, showing residues of HD subdomain only. Small coloured bars beneath the sequence scale are used to indicate the positions of prolines (pale green) and overlapped or unassigned signals (pink). Error bars were derived as described in Materials and Methods.

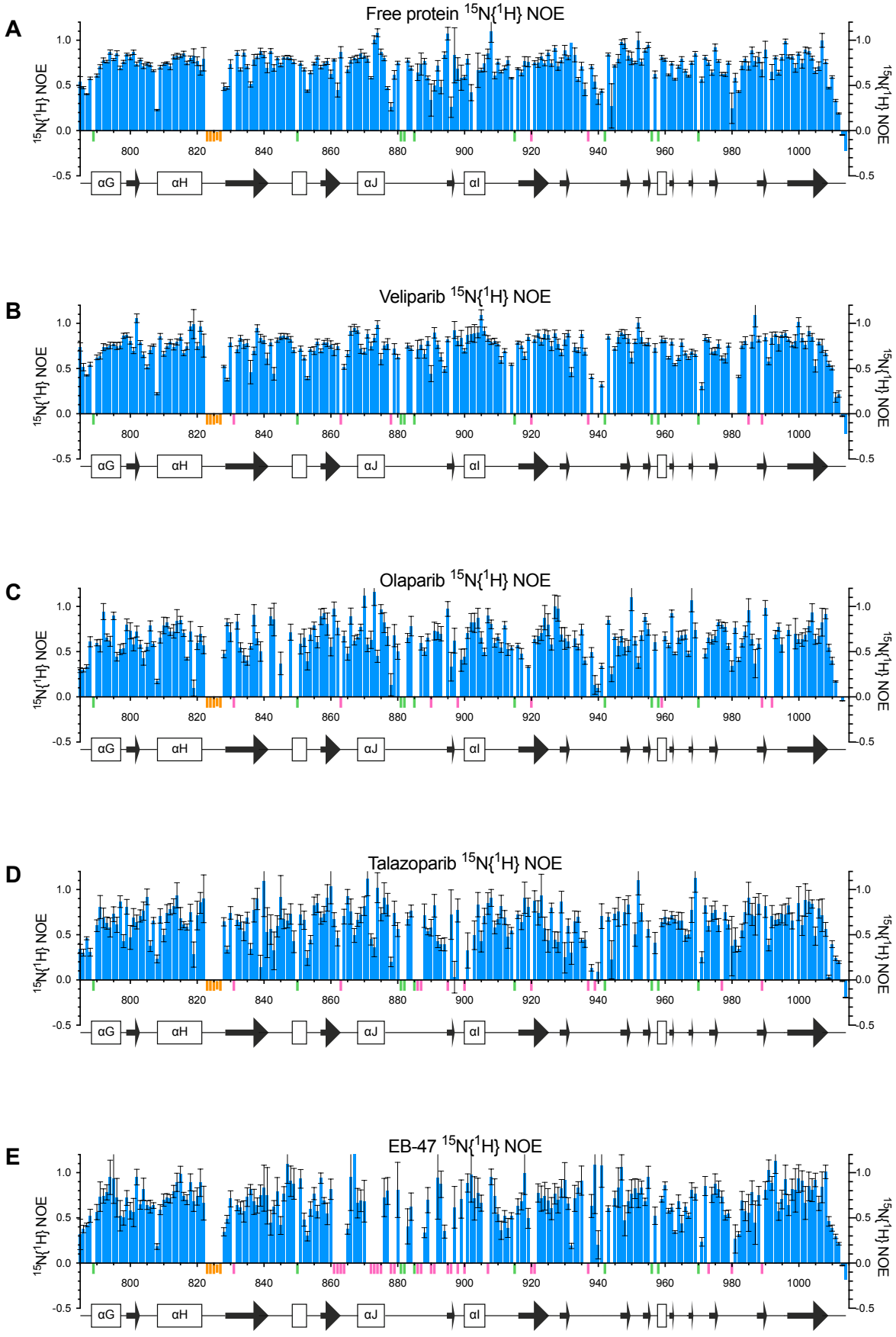

Supplementary Figure S9. Steady-state {^{1}H} ^{15}N NOE data recorded at 25°C and 800 MHz for A) PARP-1 CAT domain and its complexes with B) veliparib, C) olaparib, D) talazoparib and E) EB-47, showing residues of ART subdomain only. Small coloured bars beneath the sequence scale are used to indicate the positions of prolines (pale green), overlapped or unassigned signals (pink) and the Ala823-Asn827 loop for which no signals were seen in any spectrum (orange). Error bars were derived as described in Materials and Methods.

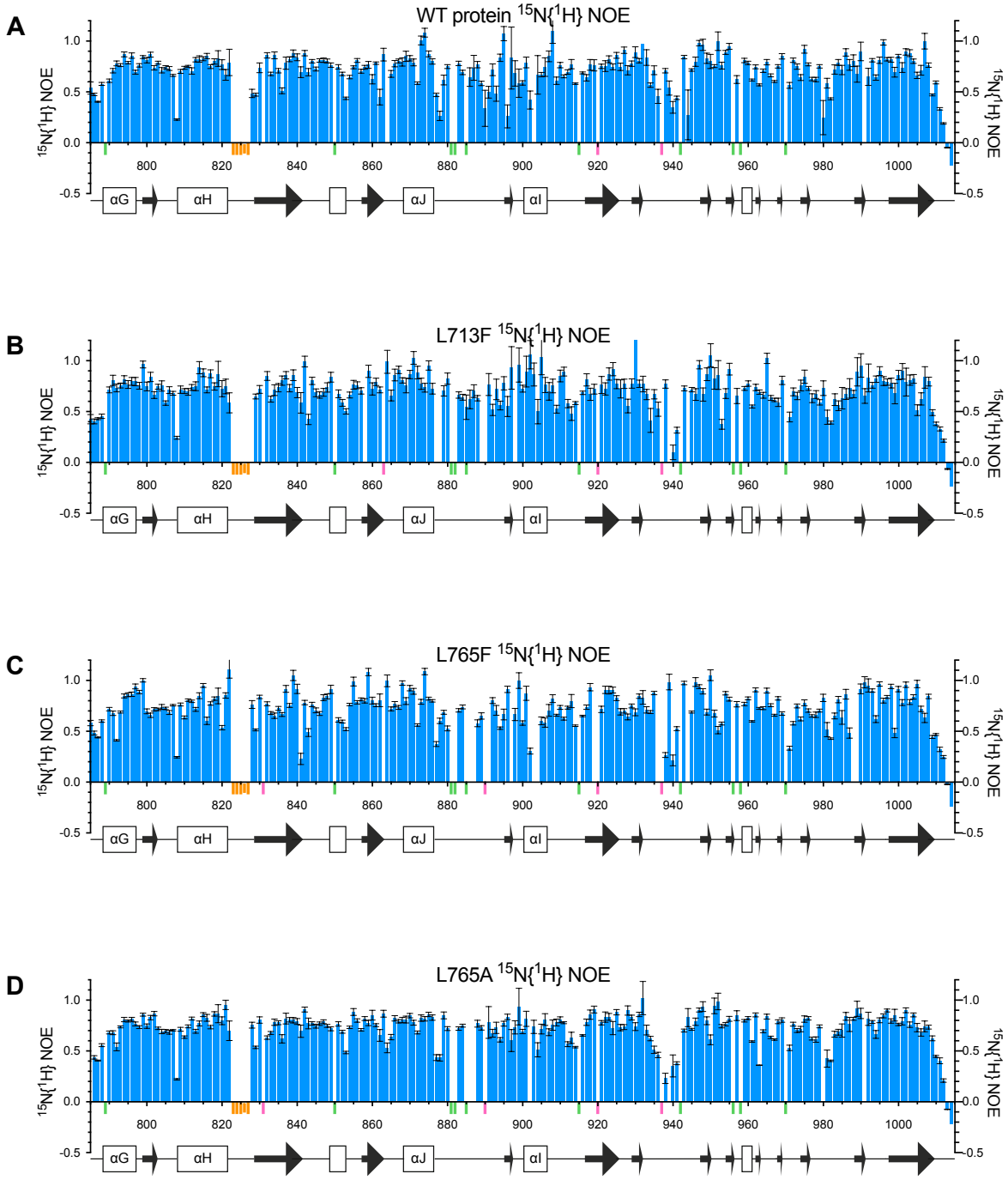

Supplementary Figure S10. Steady-state $\{^{1}H\}$ ^{15}N NOE data recorded at 25°C and 800 MHz for A) WT PARP-1 CAT domain and its point mutants B) L713F, C) L765F and D) L765A, showing residues of ART subdomain only. Small coloured bars beneath the sequence scale are used to indicate the positions of prolines (pale green), overlapped or unassigned signals (pink) and the Ala823-Asn827 loop for which no signals were seen in any spectrum (orange). Error bars were derived as described in Materials and Methods.

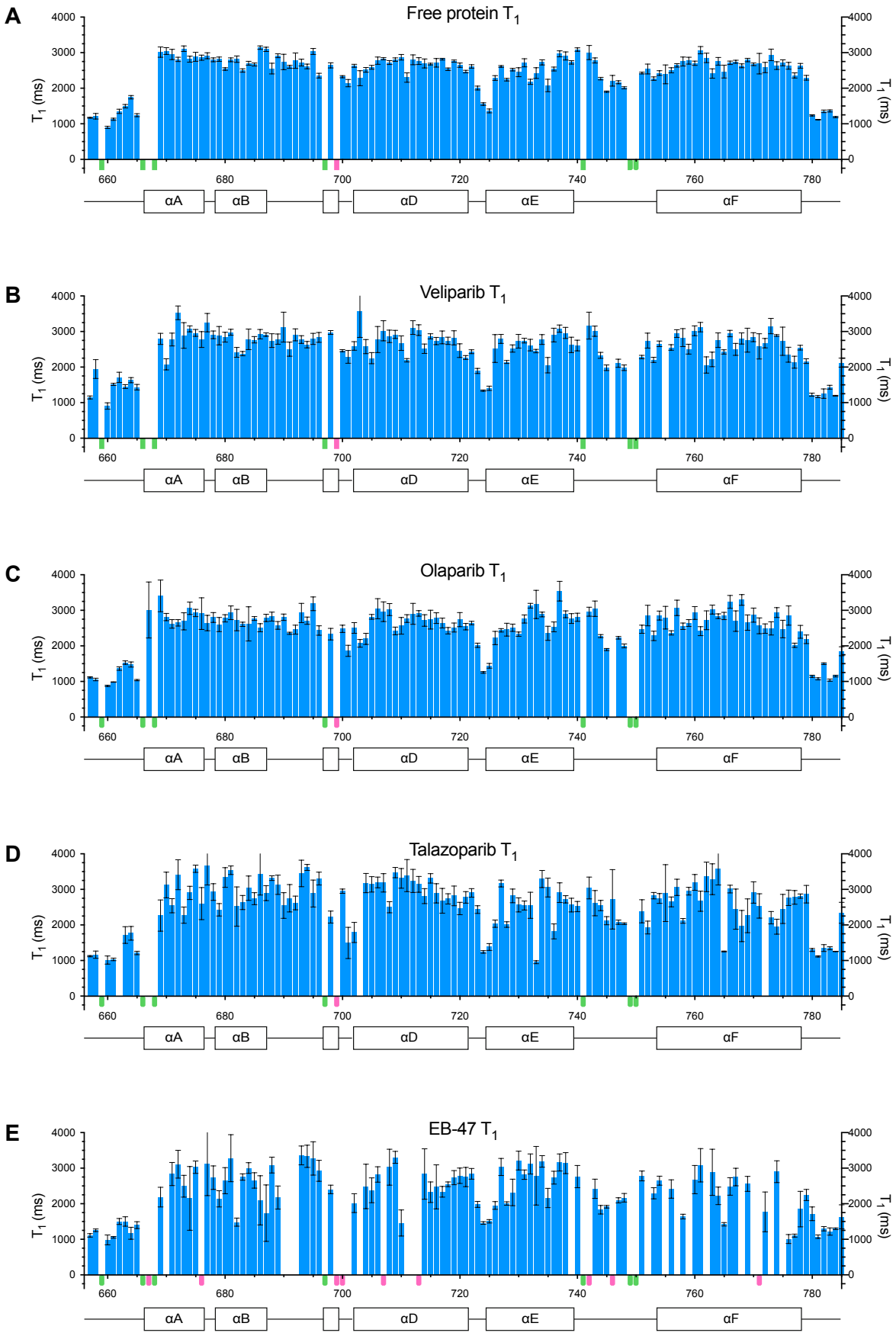

Supplementary Figure S11. ^{15}N longitudinal relaxation time (T_1) data recorded at 25°C and 800 MHz for A) PARP-1 CAT domain and its complexes with B) veliparib, C) olaparib, D) talazoparib and E) EB-47, showing residues of HD subdomain only. Small coloured bars beneath the sequence scale are used to indicate the positions of prolines (pale green) and overlapped or unassigned signals (pink). Error bars were derived as described in Materials and Methods.

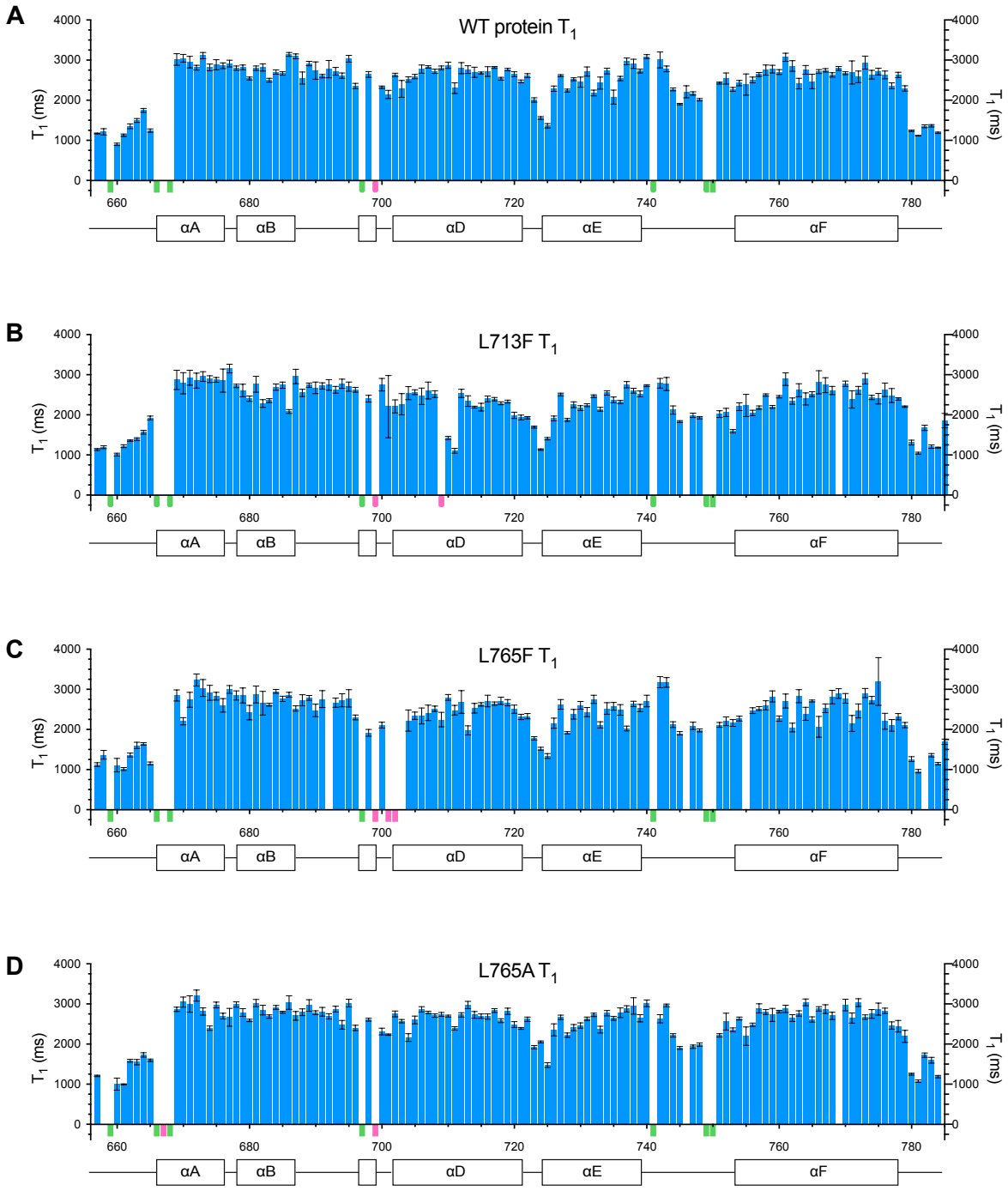

Supplementary Figure S12. ^{15}N longitudinal relaxation time (T_1) data recorded at 25°C and 800 MHz for A) WT PARP-1 CAT domain and its point mutants B) L713F, C) L765F and D) L765A, showing residues of HD subdomain only. Small coloured bars beneath the sequence scale are used to indicate the positions of prolines (pale green) and overlapped or unassigned signals (pink). Error bars were derived as described in Materials and Methods.

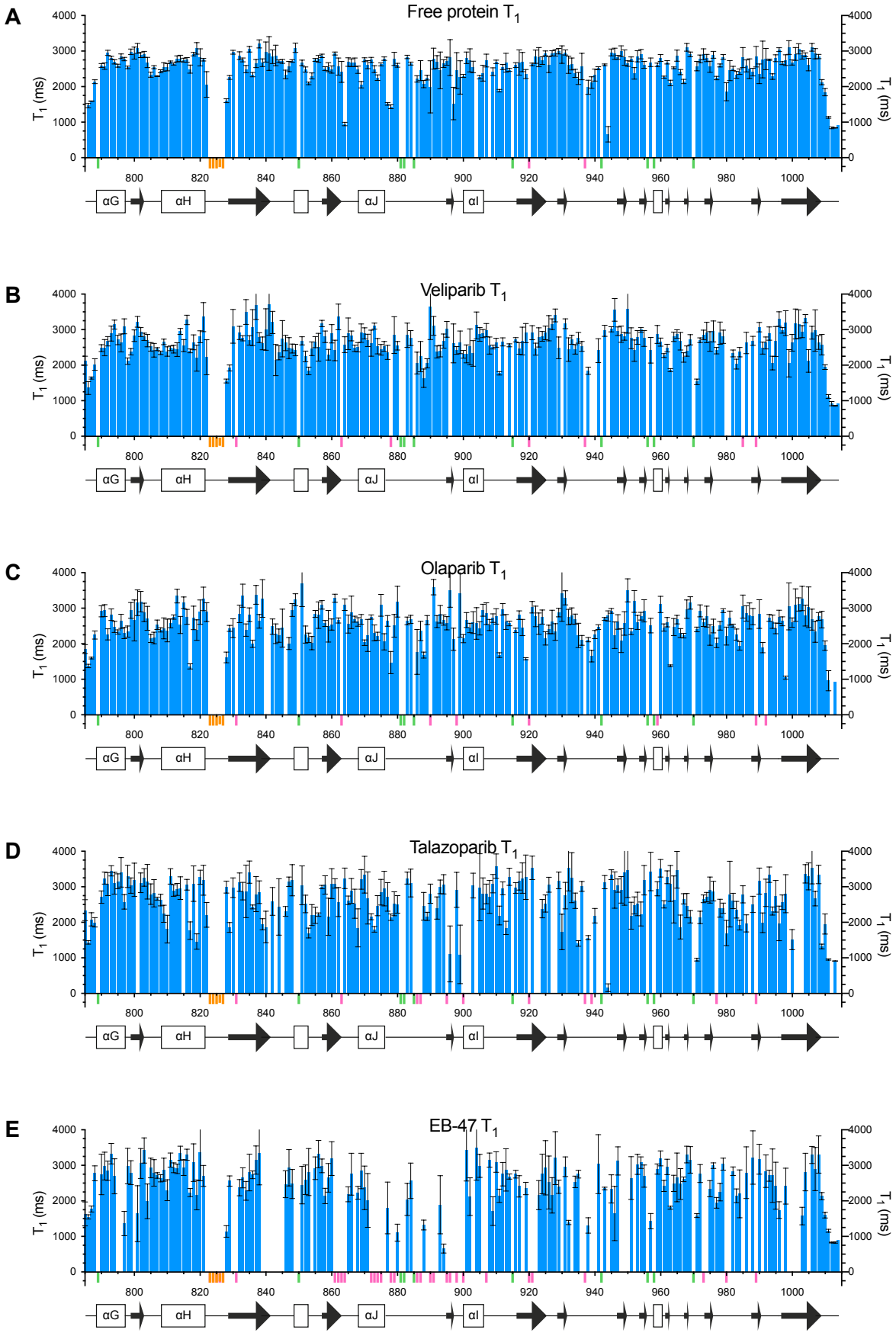

Supplementary Figure S13. ^{15}N longitudinal relaxation time (T_1) data recorded at 25°C and 800 MHz for A) PARP-1 CAT domain and its complexes with B) veliparib, C) olaparib, D) talazoparib and E) EB-47, showing residues of ART subdomain only. Small coloured bars beneath the sequence scale are used to indicate the positions of prolines (pale green), overlapped or unassigned signals (pink) and the Ala823-Asn827 loop for which no signals were seen in any spectrum (orange). Error bars were derived as described in Materials and Methods.

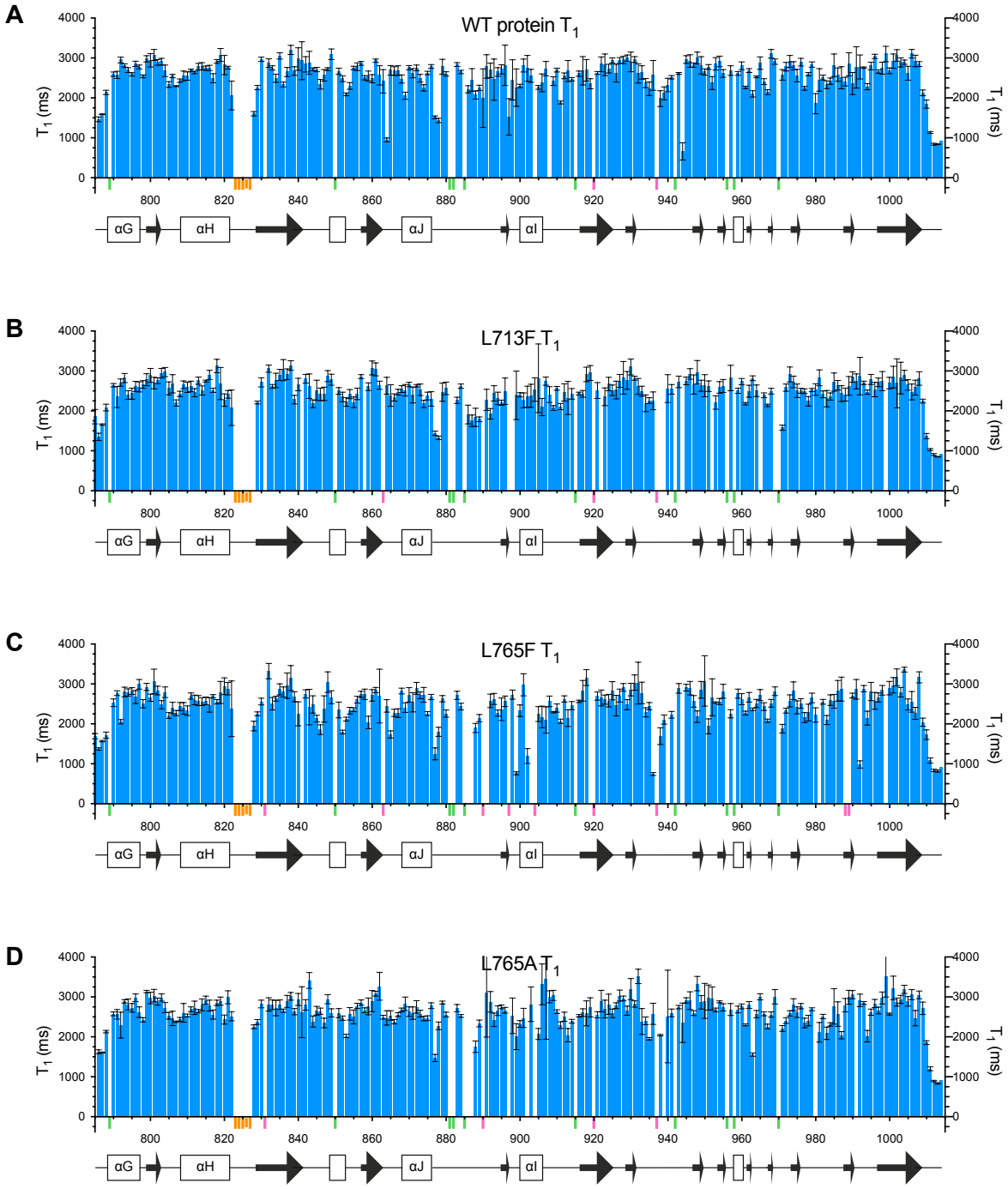

Supplementary Figure S14. ^{15}N longitudinal relaxation time (T_1) data recorded at 25°C and 800 MHz for A) WT PARP-1 CAT domain and its point mutants B) L713F, C) L765F and D) L765A, showing residues of ART subdomain only. Small coloured bars beneath the sequence scale are used to indicate the positions of prolines (pale green), overlapped or unassigned signals (pink) and the Ala823-Asn827 loop for which no signals were seen in any spectrum (orange). Error bars were derived as described in Materials and Methods.

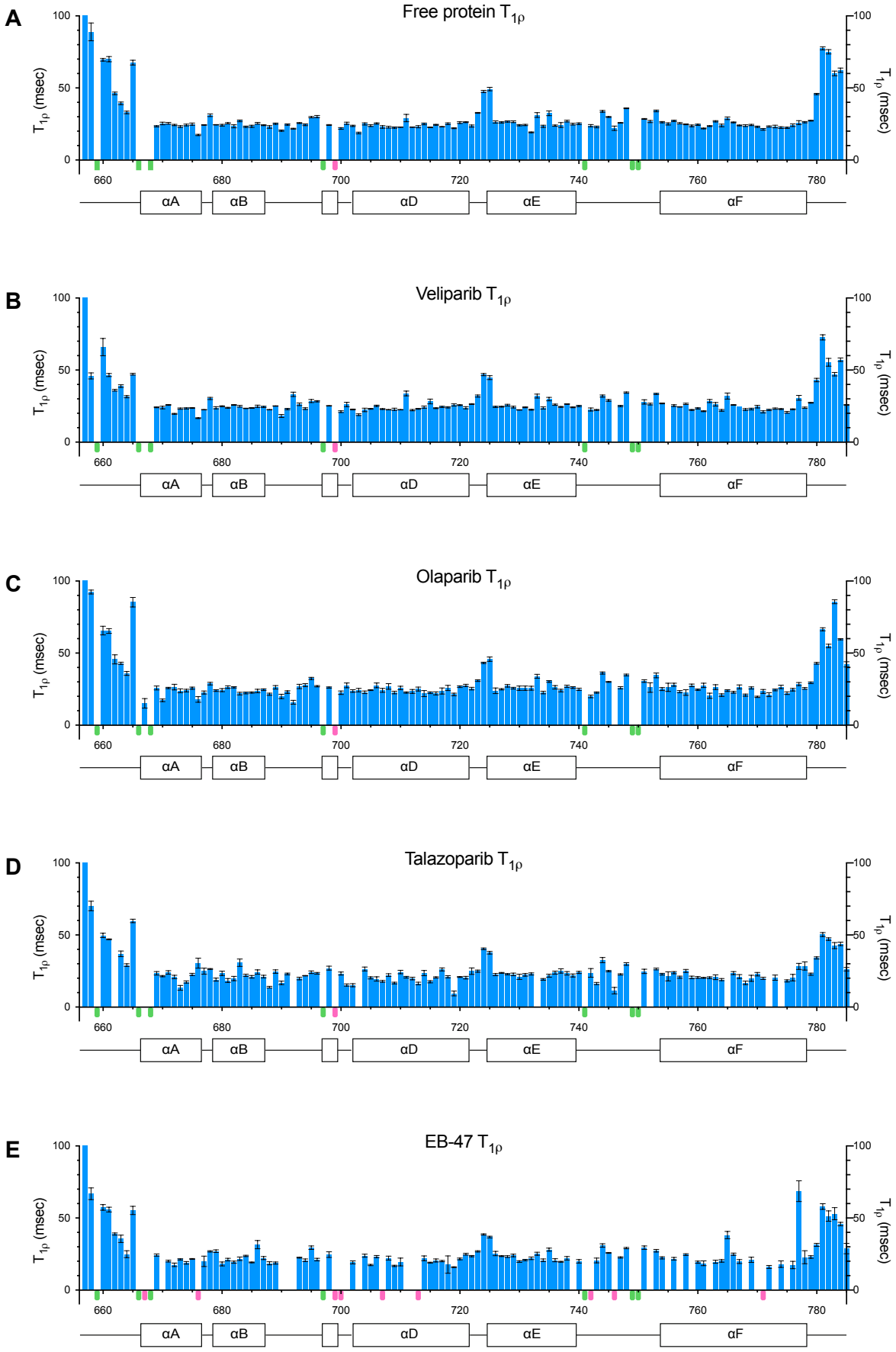

Supplementary Figure S15. ^{15}N spin-locked relaxation time ($T_{1\rho}$) data recorded at 25°C and 800 MHz for A) PARP-1 CAT domain and its complexes with B) veliparib, C) olaparib, D) talazoparib and E) EB-47, showing residues of HD subdomain only. Small coloured bars beneath the sequence scale are used to indicate the positions of prolines (pale green) and overlapped or unassigned signals (pink). Error bars were derived as described in Materials and Methods.

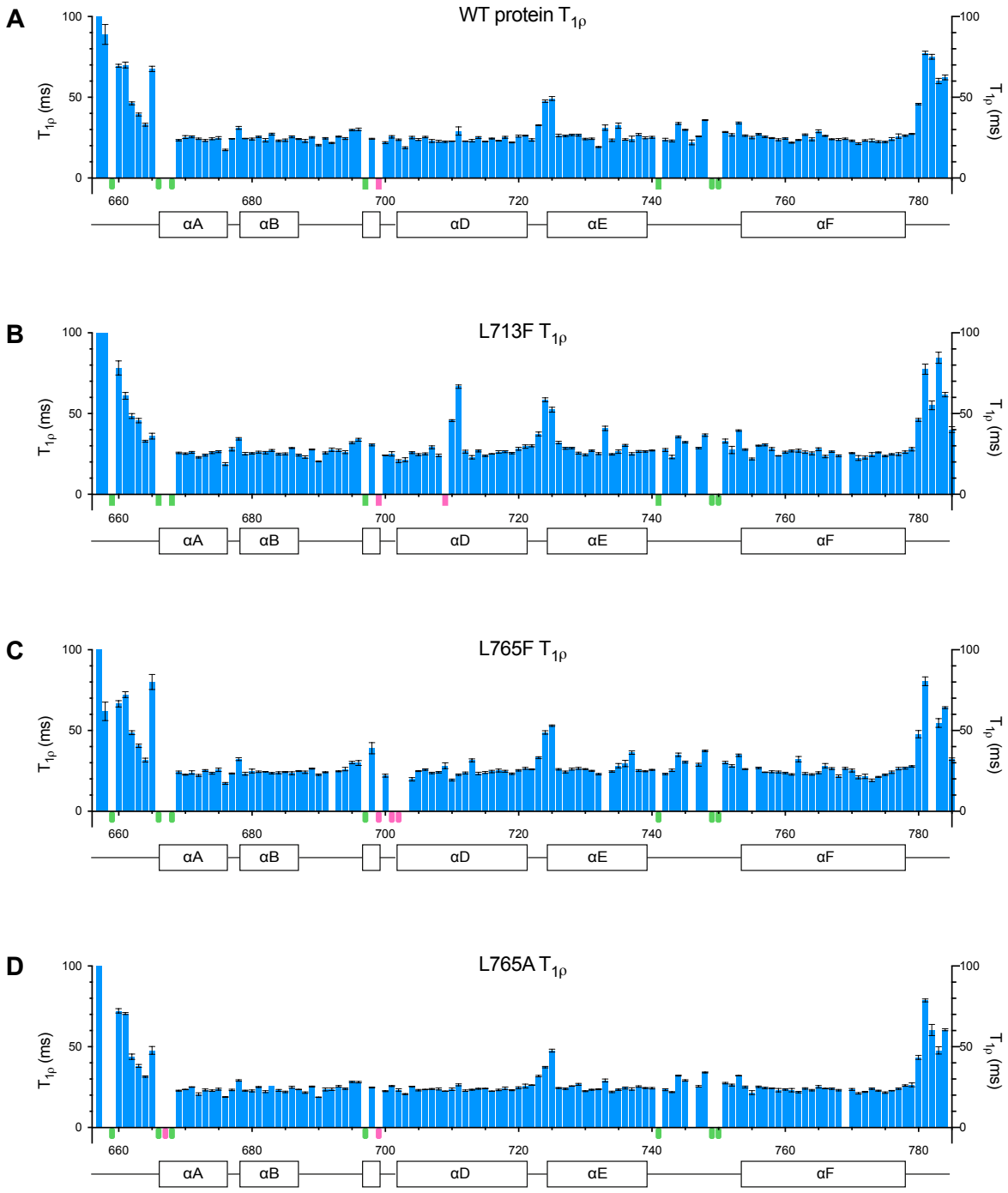

Supplementary Figure S16. ^{15}N spin-locked relaxation time ($T_{1\rho}$) data recorded at 25°C and 800 MHz for A) WT PARP-1 CAT domain and its point mutants B) L713F, C) L765F and D) L765A, showing residues of HD subdomain only. Small coloured bars beneath the sequence scale are used to indicate the positions of prolines (pale green) and overlapped or unassigned signals (pink). Error bars were derived as described in Materials and Methods.

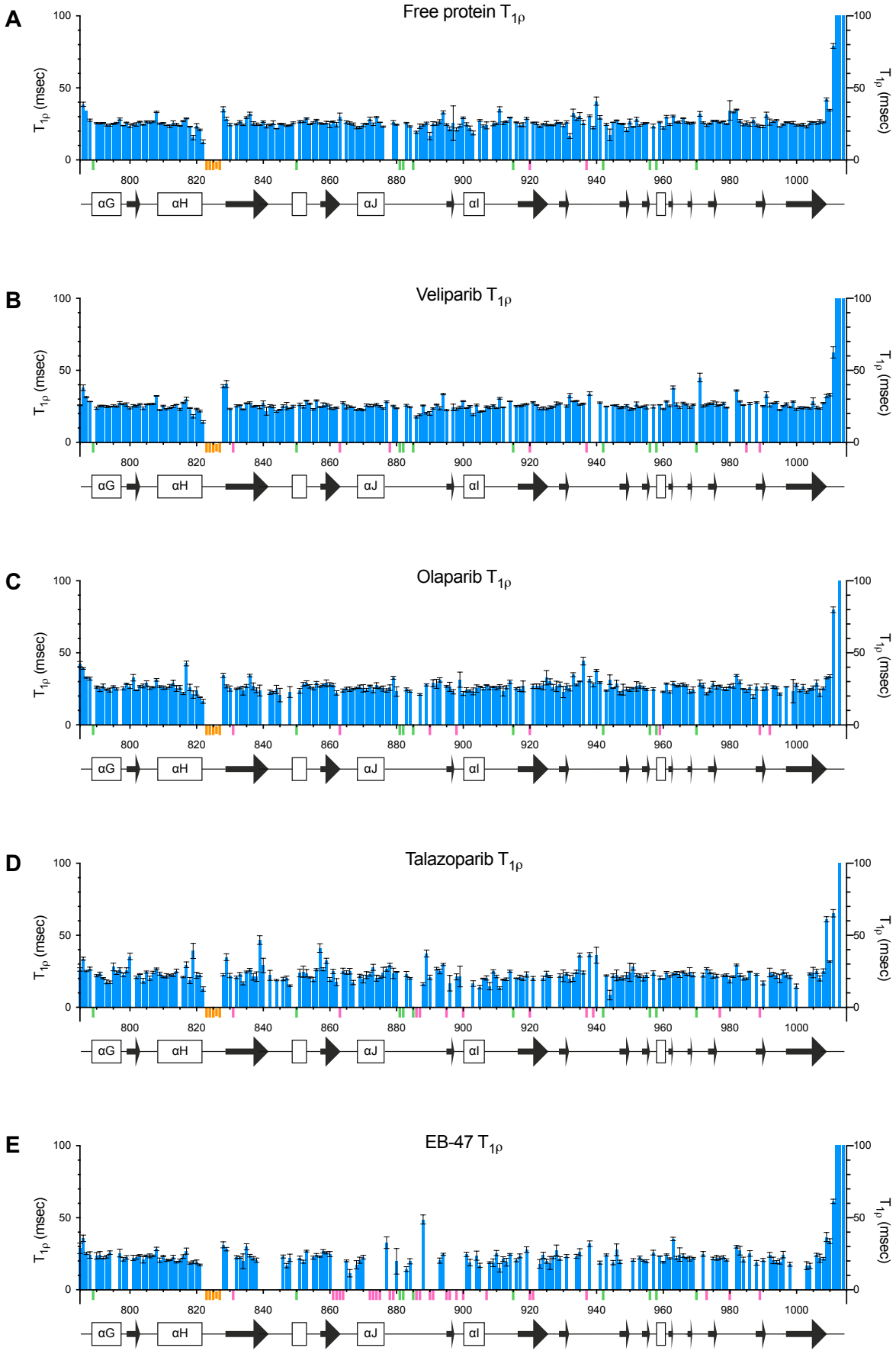

Supplementary Figure S17. ^{15}N spin-locked relaxation time ($T_{1\rho}$) data recorded at 25°C and 800 MHz for A) PARP-1 CAT domain and its complexes with B) veliparib, C) olaparib, D) talazoparib and E) EB-47, showing residues of ART subdomain only. Small coloured bars beneath the sequence scale are used to indicate the positions of prolines (pale green), overlapped or unassigned signals (pink) and the Ala823-Asn827 loop for which no signals were seen in any spectrum (orange). Error bars were derived as described in Materials and Methods.

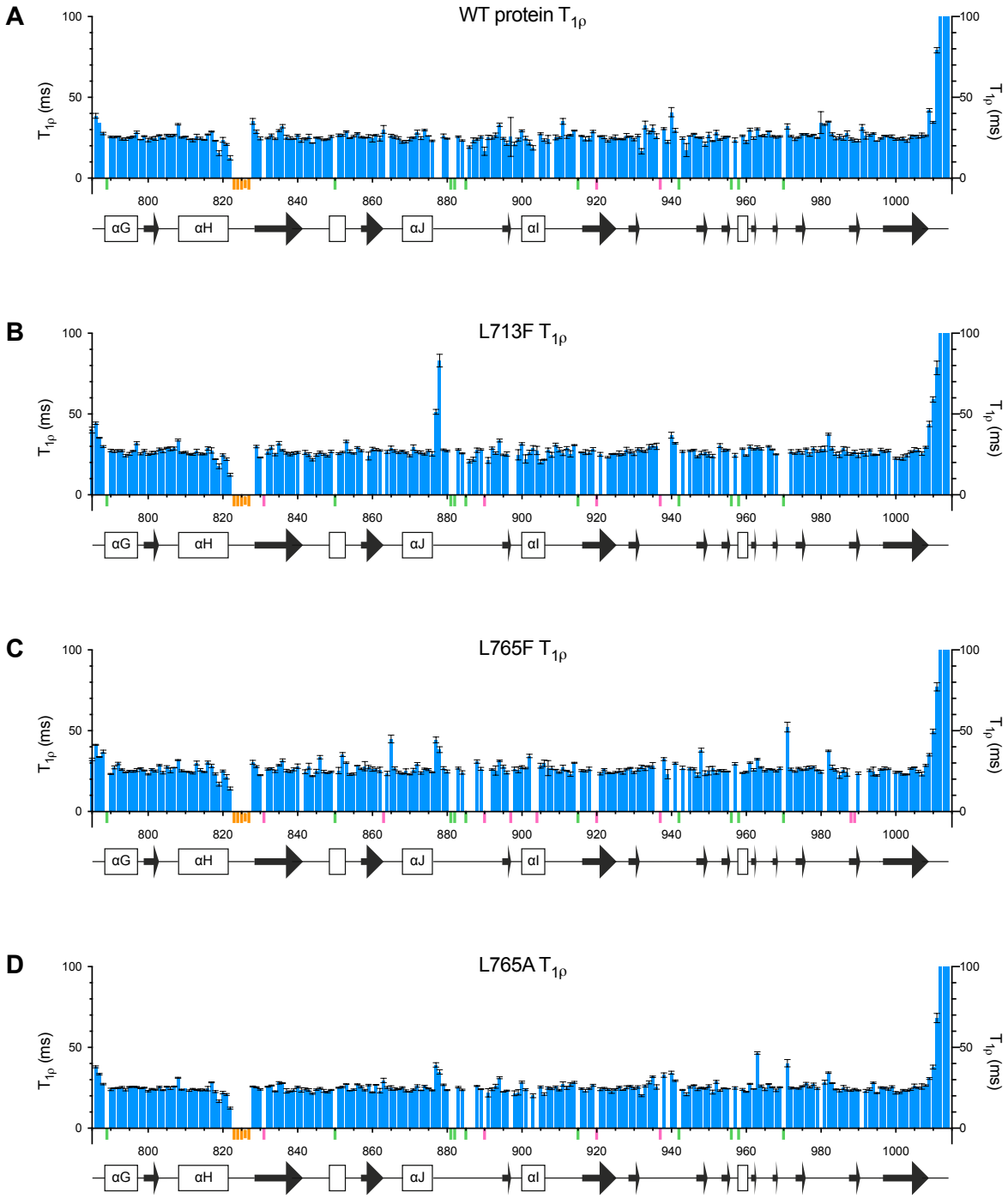

Supplementary Figure S18. ^{15}N spin-locked relaxation time ($T_{1\rho}$) data recorded at 25°C and 800 MHz for A) WT PARP-1 CAT domain and its point mutants B) L713F, C) L765F and D) L765A, showing residues of ART subdomain only. Small coloured bars beneath the sequence scale are used to indicate the positions of prolines (pale green), overlapped or unassigned signals (pink) and the Ala823-Asn827 loop for which no signals were seen in any spectrum (orange). Error bars were derived as described in Materials and Methods.

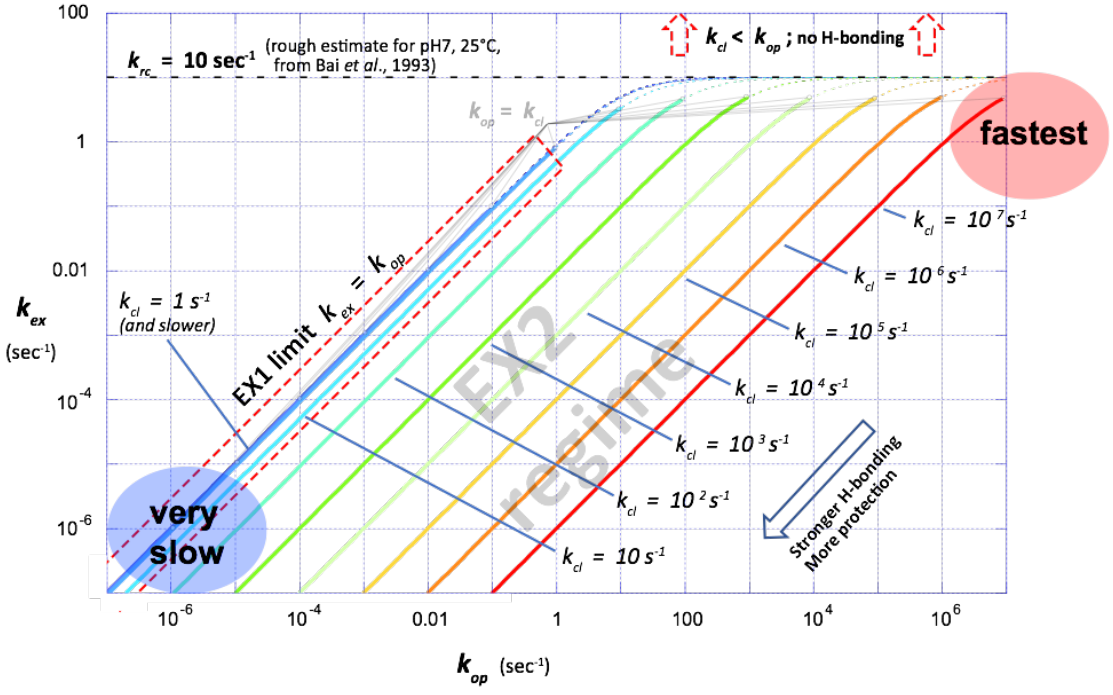

Supplementary Figure S19. Relationship between NH solvent exchange rates and conformational fluctuation rates. The figure shows plots of NH solvent exchange rate constant k_{ex} against the conformational opening rate constant k_{op} calculated using Eq (1) (defined below) for different values of the conformational closing rate constant k_{cl}, with all variables in the range 10^{-7} to 10^{7}.

i) Theory:

The fastest that an NH group can exchange with solvent corresponds to the "random coil" rate, which is the rate for an NH that experiences no protection through intramolecular hydrogen bonding; this is characterised by the rate constant k_{rc} (see point v) below). Participation in intramolecular hydrogen bonds within a folded structure retards this rate to an extent that depends on the strength of the hydrogen bond. This behaviour is usually represented using the simplified reaction scheme:

$$\mathrm{NH_{cl}} \underset{k_{cl}}{\overset{k_{op}}{\rightleftharpoons}} \mathrm{NH_{op}} \xrightarrow{k_{rc}} \mathrm{ND}$$

where k_{op} and k_{cl} are respectively the rate constants for opening and closing of the hydrogen-bonded state and it is assumed that exchange can only take place in the open state; each of these rate constants, and indeed the nature of the open state, is specific for a particular NH (also, each open state could itself comprise an ensemble of states, the properties of which are effectively averaged in this formalism). The solvent exchange rate constant k_{ex} is then given by (1):

$$k_{ex} = \frac{k_{op}k_{rc}}{k_{cl}+k_{op}+k_{rc}} \qquad (1)$$

Often this equation appears without the term k_{op} in the denominator, e.g. in (2), corresponding to the assumption that all hydrogen bonds are strong, $k_{cl} \gg k_{op}$; however, here it is of interest to plot the behaviour for both strong and weak hydrogen bonds so the k_{op} term on the lower line is retained. In the figure, those parts of the curves for which $k_{cl} > k_{op}$ (implying that the closed form containing the hydrogen bond predominates) are shown using thick solid lines, while those parts for which $k_{cl} < k_{op}$ (implying that the open form where there is no hydrogen bond predominates) are shown using thin dotted lines.

Because solvent exchange is a chemical reaction, it shows strong dependence on solution conditions, particularly pH and temperature, and in addition is sensitive to the chemical nature of nearby sidechains. For an amide group in a random coil conformation, i.e. one that is "unprotected" as it participates only in transient hydrogen bonds with solvent, the random coil rate solvent exchange constant k_{rc} can be roughly predicted from model compound studies (3); for a protein at pH 7.0 and 25 °C, k_{rc} would be expected to be very roughly 10 s^{-1}, with variations of up to about a factor of ten in either direction depending on sequence context. This is the value that was used in the simulations shown in the figure; for more details see point vi) below.

ii) EX2 and EX1 limits:

Two limiting cases are usually considered, which differ according to whether it is the first step (structural opening) or second step (exchange) that is rate-limiting; the first limit is referred to as EX1 and the second as EX2 (4). By far the commonest situation is for exchange to be in or near the EX2 limit, where structural fluctuations are much faster than intrinsic exchange, $k_{cl} + k_{op} \gg k_{rc}$, so that Eq. 1 becomes:

$$k_{ex} = \frac{k_{op}}{k_{cl}+k_{op}} k_{rc} = f_{op} k_{rc} \qquad \text{(EX2)} \qquad (2)$$

In effect, this implies that an equilibrium is rapidly established between the closed and open states, and the observed exchange rate then reflects both the fractional abundance of the opened state (f_{op}) and the rate of exchange events it undergoes once formed. For hydrogen bonds strong enough that $k_{cl} \gg k_{op}$, the EX2 condition is often written as

$$k_{ex} = \frac{k_{op}}{k_{cl}} k_{rc} = K_{op} k_{rc} \qquad \text{(EX2)} \qquad (3)$$

where K_{op} is the equilibrium constant for the pre-equilibrium between open and closed states.

For extremely slow rates, exchange can reach the EX1 limit, $k_{cl} + k_{op} \ll k_{rc}$, and then Eq. 1 becomes simply:

$$k_{ex} = k_{op} \qquad \text{(EX1)} \qquad (4)$$

On the figure, the EX1 limit manifests as the coalescence into a single line of all of the curves for which k_{cl} < 1 s^{-1}, in the region marked with a dashed red box. The EX2 limit is less obviously visualisable on the figure, but corresponds to those curves for which k_{cl} > 100 s^{-1} (i.e. the bulk of the remainder of the plot), where increasing k_{cl} leads to a proportionate movement of the k_{ex} vs k_{op} line. It may be noted that, formally, Eq. 1 is an approximation, since between the EX1 and EX2 limits (here corresponding approximately to the range 1 s^{-1} < k_{cl} < 100 s^{-1}) exchange follows a bi-exponential rate that cannot be represented analytically using a single rate constant (5); however, this complication is often ignored.

iii) Fastest events:

The NH protons that undergo the fastest solvent exchange are those situated in particularly mobile loops, where they participate only very weakly or not at all in intra-molecular hydrogen bonding; they are largely or completely unprotected from solvent exchange and consequently exchange at or near the random-coil rate. Under the conditions of the present study (25 °C and pH7), k_{rc} is roughly 10 s^{-1} (see vi below). However, the rate of underlying conformational motions for such protons is very much faster. For such motions to be detected in ^{15}N relaxation experiments, they must be faster than overall molecular tumbling, which for PARP-1 CAT domain at 25 °C in the present study has a correlation time of $\tau_c \approx$ 25 ns (see main text).

In other words, in such cases there are *at least seven orders of magnitude* difference between the rates of NH proton solvent exchange and the underlying rates of conformational exchange events involving those protons. This corresponds roughly to the part of the plot highlighted in red labelled "fastest". In this regime it would be expected that the conformational motions of individual peptide groups are largely un-coordinated with those of their neighbours, and any transient making or breaking of intramolecular hydrogen bonds involving these peptides would probably be largely or completely non-cooperative in nature.

iv) Slowest events:

In contrast, NH protons that exchange with solvent the most slowly can be at the EX1 limit, where the rate of solvent NH proton exchange is *equal to* the rate of the underlying conformational processes responsible for transiently breaking hydrogen bonds. Such cases could lie within the part of the plot highlighted in blue labelled "very slow" (though still slower cases of exchange corresponding to still stronger hydrogen bonds, and which would lie outside the limits of this plot, are also entirely possible). Hydrogen bonds involved in these processes are very strong indeed, and the processes that break them are likely to be highly co-operative in nature, involving the disruption of large sections of the structure (2,6,7); in the limit, for NH protons involved in the very strongest hydrogen bonds in the most stable of protein structures, solvent exchange can require global unfolding of the entire structure (8). Cases of EX1 exchange are relatively rare, although working at high pH makes EX1 more likely as it increases greatly the random coil exchange rate (2).

v) Between the extremes:

The great majority of hydrogen-bonded NH protons characterised in exchange studies fall between the limiting behaviours just described, and are mostly within the EX2 regime. Generalisations are difficult, but it seems reasonable to expect that the trend from fastest to slowest solvent exchange would correspond very approximately to a trend from least to most co-operativity in the conformational processes underlying exchange; for the great majority of hydrogen bonds, the conformational fluctuations required for transient opening will involve some other portions of nearby structure that are interconnected in the hydrogen bonding network, and the stronger the hydrogen bond, the larger the "structural reach" of such co-operative events is likely to have to be (8). Implications for the relationship between solvent exchange rates and rates of the underlying conformational fluctuations causing exchange are also hard to predict, but one may expect that the slower the exchange, the smaller is likely to be the extent by which conformational fluctuation rates are faster than solvent exchange. Even so, the EX2 regime covers a very broad range of NH solvent exchange rates, and in the majority of cases it is likely that the underlying conformational fluctuations that drive exchange are significantly faster than solvent exchange itself, potentially by orders of magnitude.

Without measured data concerning k_{op} and k_{cl}, quantitative statements are impossible. However, the purpose of the analysis presented here is to extend the caution given elsewhere in the literature, e.g. in (2,7), against assuming that measured solvent exchange rates are similar to the rates of underlying conformational transitions responsible for that exchange; this is highly unlikely to be the case except for the very slowest exchanging NH protons that are at or near the EX1 limit.

vi) Random coil exchange rate at pH7 and 25 °C:

The prediction for k_{rc} used in the simulations was obtained from the data and analysis in Bai *et al*. (3) as follows: For a random coil amide group, the solvent NH exchange rate constant uncorrected for neighbouring sidechain effects is given by

$$k_{rc} = k_{ex} = k_A\, 10^{-pD} + k_B\, 10^{[pD-pK_D]} + k_W \qquad (4)$$

where k_A is the rate constant for acid-catalysed exchange, k_B is that for base catalysed exchange and k_W is that for water catalysed exchange. At 20 °C, the temperature for which Bai *et al*. give tabulated data, the value of K_D (the self-ionisation constant for D_2O) is 15.049 (9). At pH 7, catalysis by acid and water can be neglected, so after conversion to log units Eq. (4) becomes:

$$\log(k_{rc}) = \log(k_B) + pD - pK_D$$
$$= 10.36 + 7.4 - 15.05 = 2.71$$

where $\log(k_B)$ = 10.36 comes from Bai *et al*. Table 3 (note that rates in Bai *et al*. are all expressed in min^{-1}) and 7.4 is the value of pD corresponding to an uncorrected pH meter reading of 7.0 made with a conventional glass electrode (10). From this,

$$k_{rc} = 10^{2.62} = 513\ min^{-1} = 8.55\ s^{-1}.$$

Corrections for local sequence (see Bai *et al*. Table 2) can cause a maximal negative variation in k_B of -0.97 log units (for the NH of Ile in the sequence Ile-Pro) and maximal positive variation in k_B of +1.45 log units (for the NH of Cys in the sequence Cys-His^+). These corrections would correspond to a range in the rates between 0.91 s^{-1} and 241 s^{-1}. The average over all sidechain corrections

(ignoring COOH forms, as these would be absent at pH 7) would give -0.02 to +0.14 log units, which corresponds to a range in the rates between 8.16 s^{-1} and 11.8 s^{-1}.

Using the Arrhenius equation to correct these values from a temperature of 20 °C to 25 °C gives:

$$k_{rc}(T) = k_{rc}(293)\, exp^{(-E_a[1/T - 1/293]/R)}$$

where E_a is the activation energy for base-catalysed exchange, given as 17 kcal.mol^{-1} by Bai *et al*., and R is the gas constant, 1.985 × 10^{-3} kcal.K^{-1}.mol^{-1}, giving a correction factor of:

$$exp^{\left(\frac{-17[1/298 - 1/293]}{0.001985}\right)} = exp^{0.49} = 1.63$$

Thus, the random coil exchange rate constant at 25°C, uncorrected for sequence variations, is approximately 13.9 s^{-1}. This value was rounded to 10 s^{-1} for use in the simulations.

References for Supplementary Figure S19

1. Hvidt, A. (1964) A Discussion of the Ph Dependence of the Hydrogen-Deuterium Exchange of Proteins. *C R Trav Lab Carlsberg*, **34**, 299-317.
2. Ferraro, D.M., Lazo, N. and Robertson, A.D. (2004) EX1 hydrogen exchange and protein folding. *Biochem.*, **43**, 587-594.
3. Bai, Y., Milne, J.S., Mayne, L. and Englander, S.W. (1993) Primary structure effects on peptide group hydrogen exchange. *Proteins*, **17**, 75-86.
4. Hvidt, A. and Nielsen, S.O. (1966) Hydrogen exchange in proteins. *Adv Protein Chem*, **21**, 287-386.
5. Wedin, R.E., Delepierre, M., Dobson, C.M. and Poulsen, F.M. (1982) Mechanisms of hydrogen exchange in proteins from nuclear magnetic resonance studies of individual tryptophan indole NH hydrogens in lysozyme. *Biochem.*, **21**, 1098-1103.
6. Woodward, C.K. and Hilton, B.D. (1979) Hydrogen exchange kinetics and internal motions in proteins and nucleic acids. *Annu Rev Biophys Bioeng*, **8**, 99-127.
7. Roder, H., Wagner, G. and Wuthrich, K. (1985) Amide proton exchange in proteins by EX1 kinetics: studies of the basic pancreatic trypsin inhibitor at variable p2H and temperature. *Biochem.*, **24**, 7396-7407.
8. Englander, S.W., Sosnick, T.R., Englander, J.J. and Mayne, L. (1996) Mechanisms and uses of hydrogen exchange. *Curr Opin Struct Biol*, **6**, 18-23.
9. Covington, A.K., Robinson, R.A. and Bates, R.G. (1966) The ionization constant of deuterium oxide from 5 to 50°. *The Journal of Physical Chemistry*, **70**, 3820-3824.
10. Glasoe, P.K. and Long, F.A. (1960) Use of glass electrodes to measure acidities in deuterium oxide. *Journal of Physical Chemistry*, **64**, 188-193.

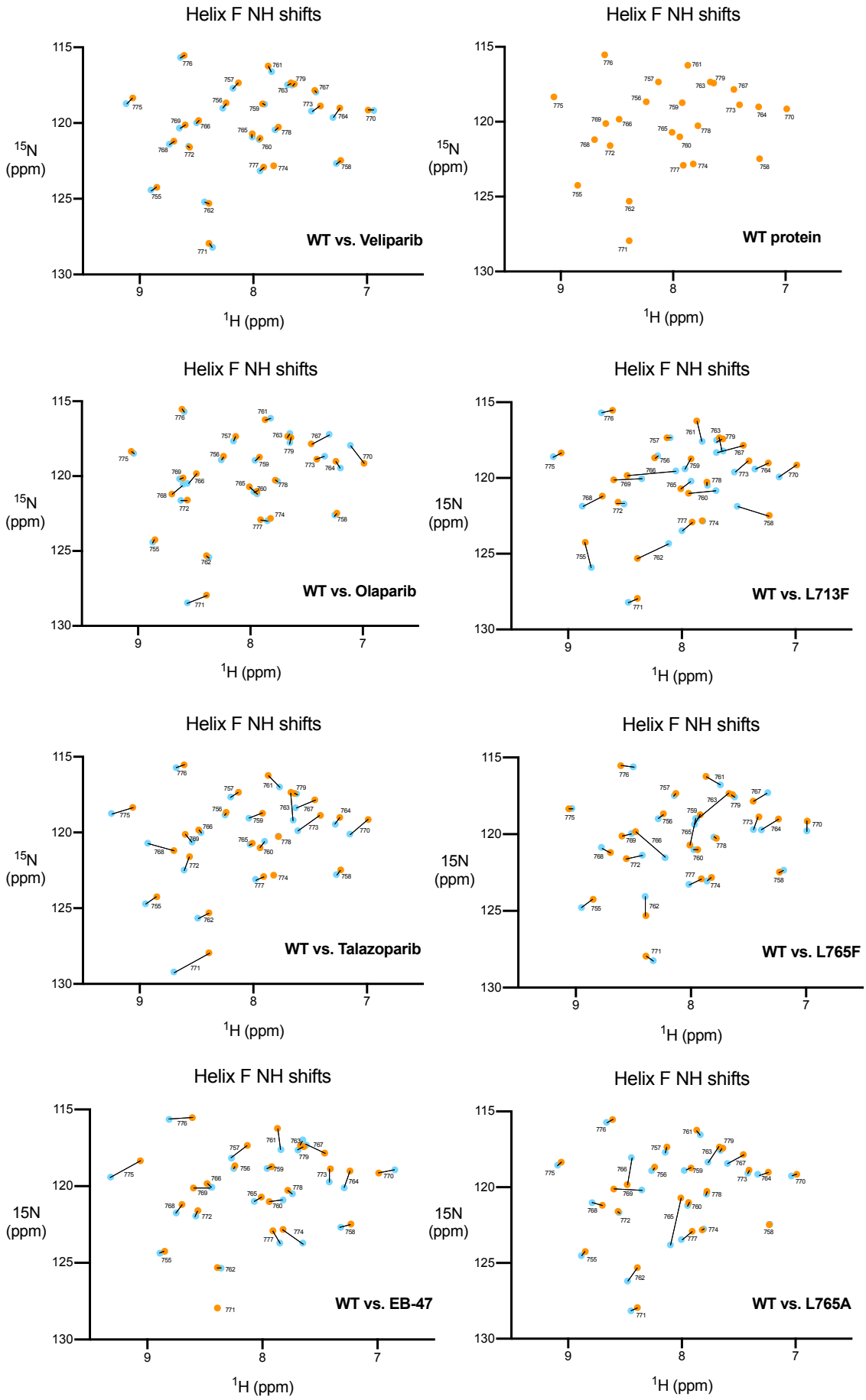

Supplementary Figure S20. Schematic [^{15}N,^{1}H] correlation plots showing chemical shift differences for the amide group ^{1}H and ^{15}N signals of residues in helix F for the comparisons indicated on the individual panels; in each case the WT free protein signal is indicated in orange and the mutant or inhibitor complex signal in light blue. The corresponding schematic for helix F of WT protein alone is also shown.

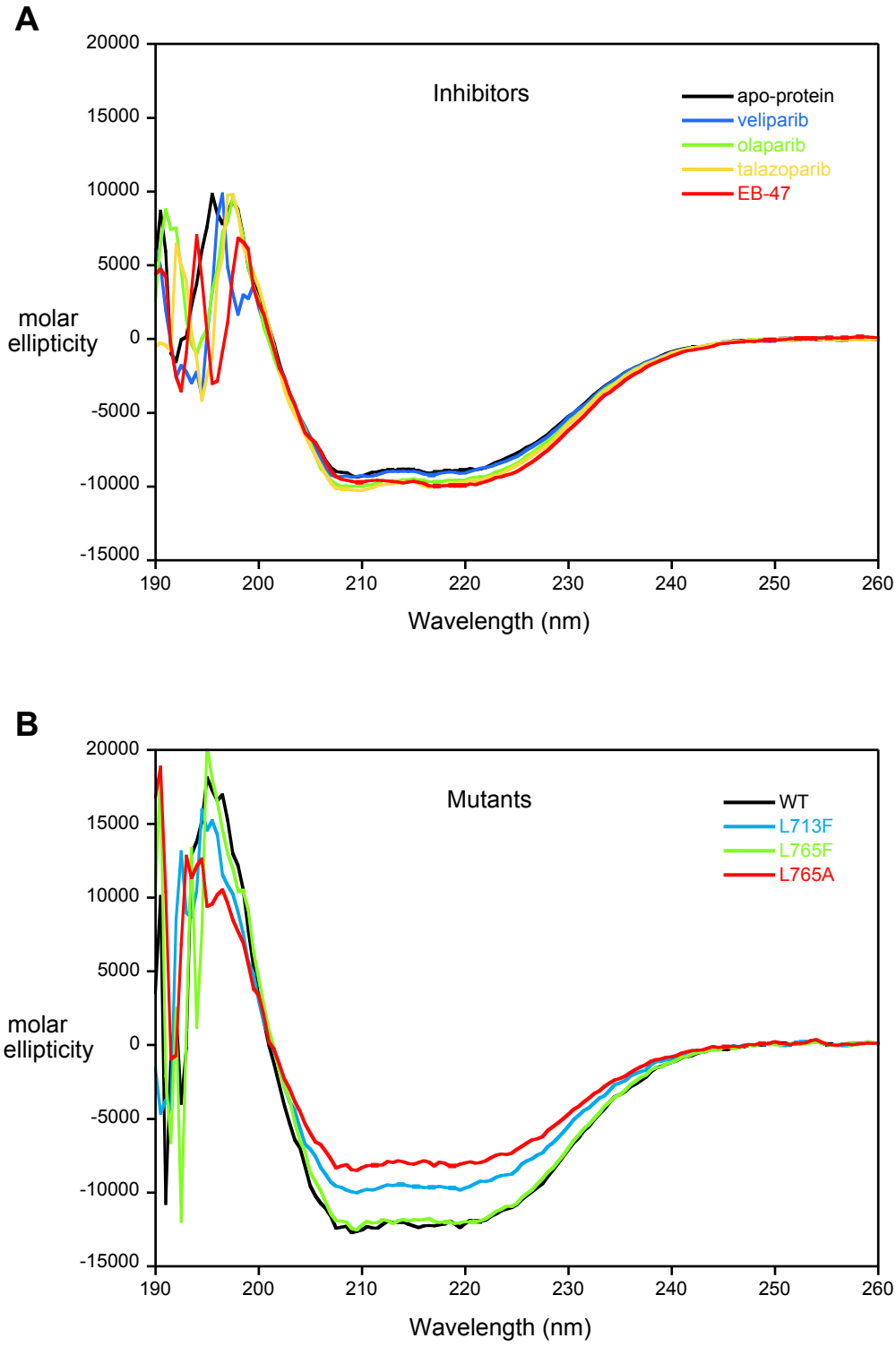

Supplementary Figure S21. CD spectra of PARP-1 CAT domain, and A) its complexes with veliparib, olaparib, talazoparib and EB-47, and B) the point mutants L713F, L765F and L765A, showing that no large-scale perturbation of secondary structure results from binding of these inhibitors or from these mutations. Apparent scaling differences amongst the spectra of the mutants probably reflect errors in estimating concentrations between these different protein samples, whereas the curves for inhibitor complexes all rely on a single protein concentration estimate. All spectra were recorded at 20°C.

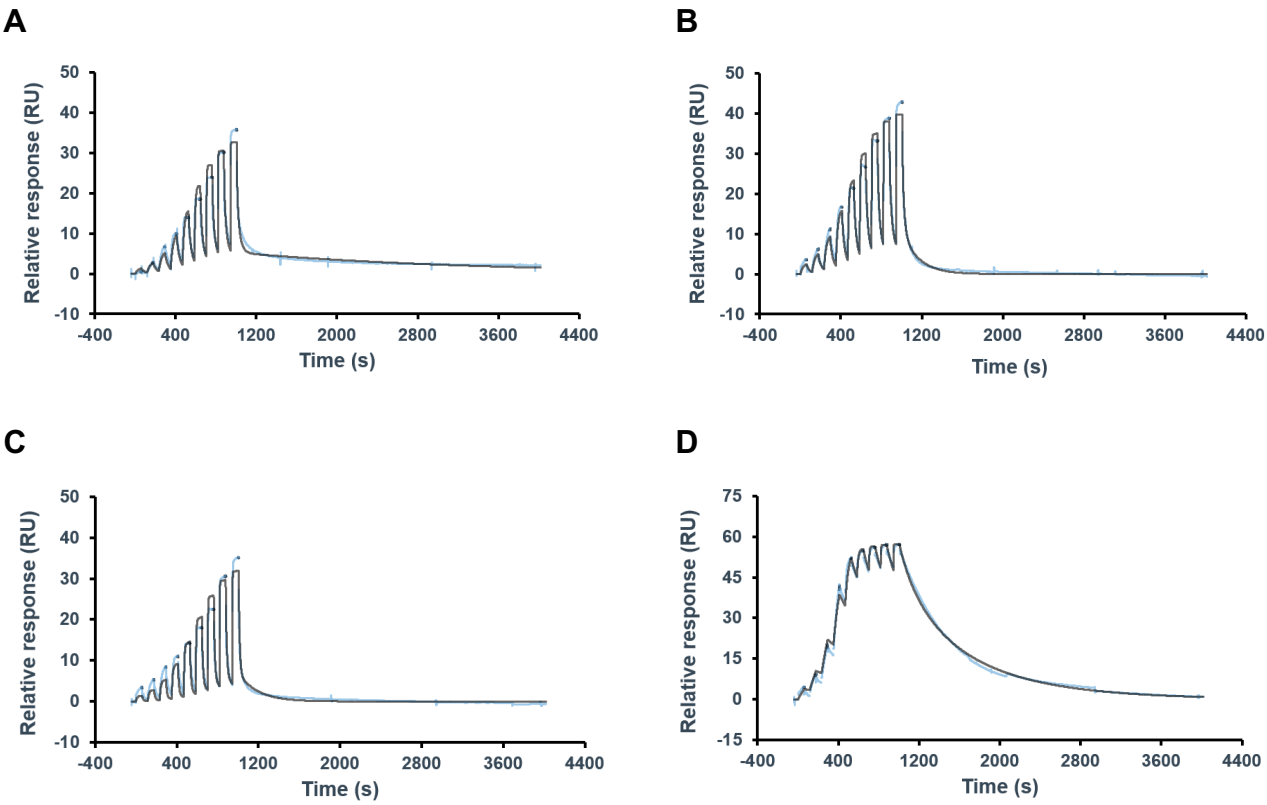

Supplementary Figure S22. Single-cycle kinetic surface plasmon resonance sensorgrams for A) PARP-1 alone, B) PARP-1 + olaparib, C) PARP-1 + veliparib and D) PARP-1 + EB-47 binding to DNA. Concentrations of PARP-1 were 0.078, 0.156, 0.313, 0.625, 1.25, 2.5, 5, 10 and 20 nM. Data were fitted to steady state for A)-C). For D, the light blue line is the SPR data, the black line is the fit to a 1:1 binding model. All sensorgrams are representative of at least three separate experiments.

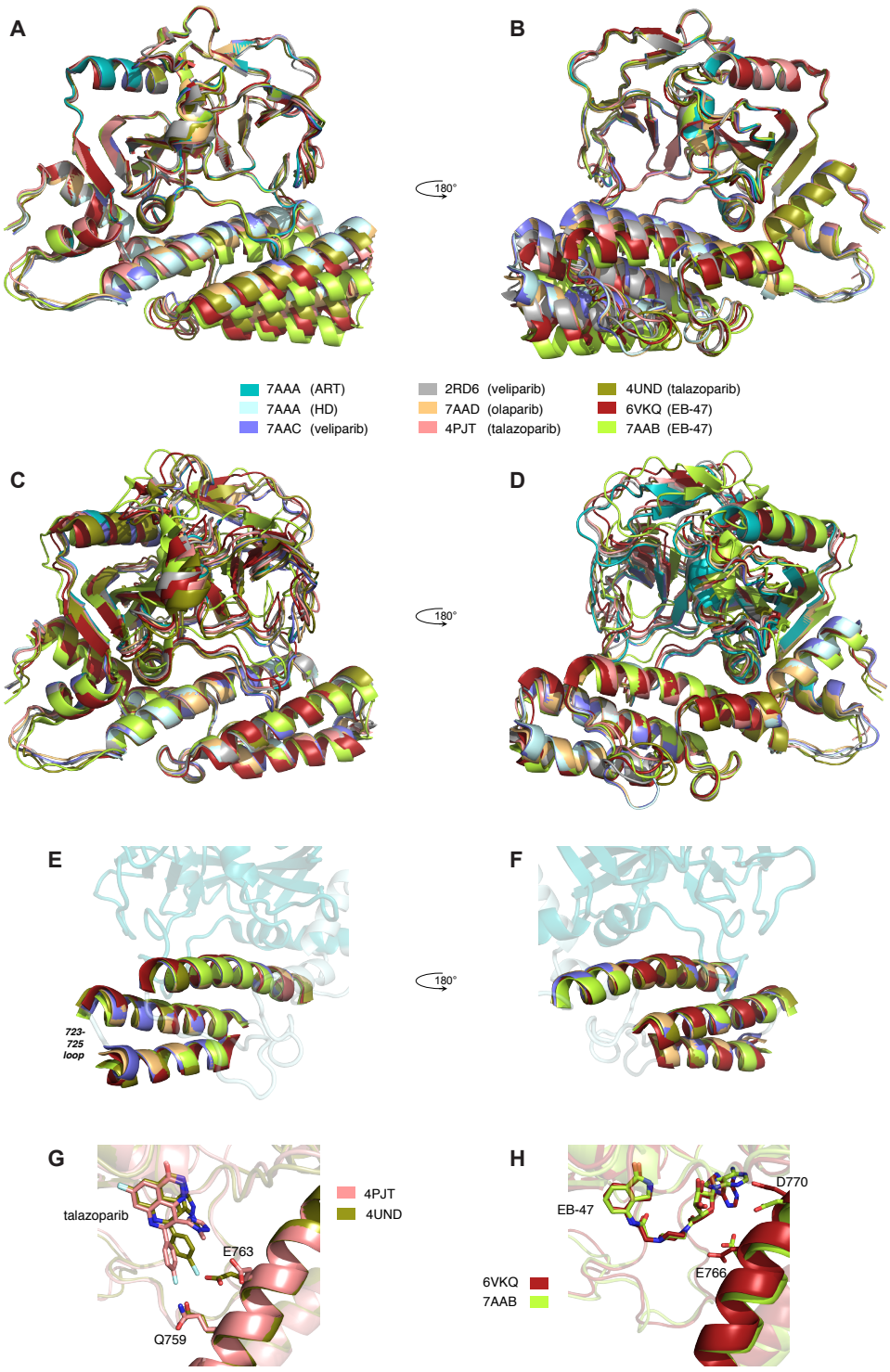

Supplementary Figure S23. Superpositions of PARP-1 CAT domain in the apo-protein and in inhibitor complexes with veliparib (PDB:7AAC and 2RD6), olaparib (PDB:7AAD), talazoparib (PDB:4PJT and 4UND) and EB-47 (PDB:7AAB and PDBB:6VKQ), in each case superposing each structure onto atoms of 7AAA. Superpositions were carried out using backbone atoms of the ART subdomain (N, Cα, C' of residues 790-936, 939-1009) (panels A and B), backbone atoms of the HD subdomain (N, Cα, C' of residues 667-721,730-743,750-779) (panels C and D), or backbone atoms of helices D, E and F (N, Cα, C' of residues 702-721,730-740,754-779) (panels E and F). N.B. The viewpoints in panels E and F are changed relative to those in panels A-D so as to facilitate viewing the helical distortions. Panels G and H show steric clashes involving sidechains of residues in helix F for the complexes with talazoparib (clashes with Gln759 and Glu763; panel G) and EB-47 (clashes with Glu766 and Asp770; panel H).

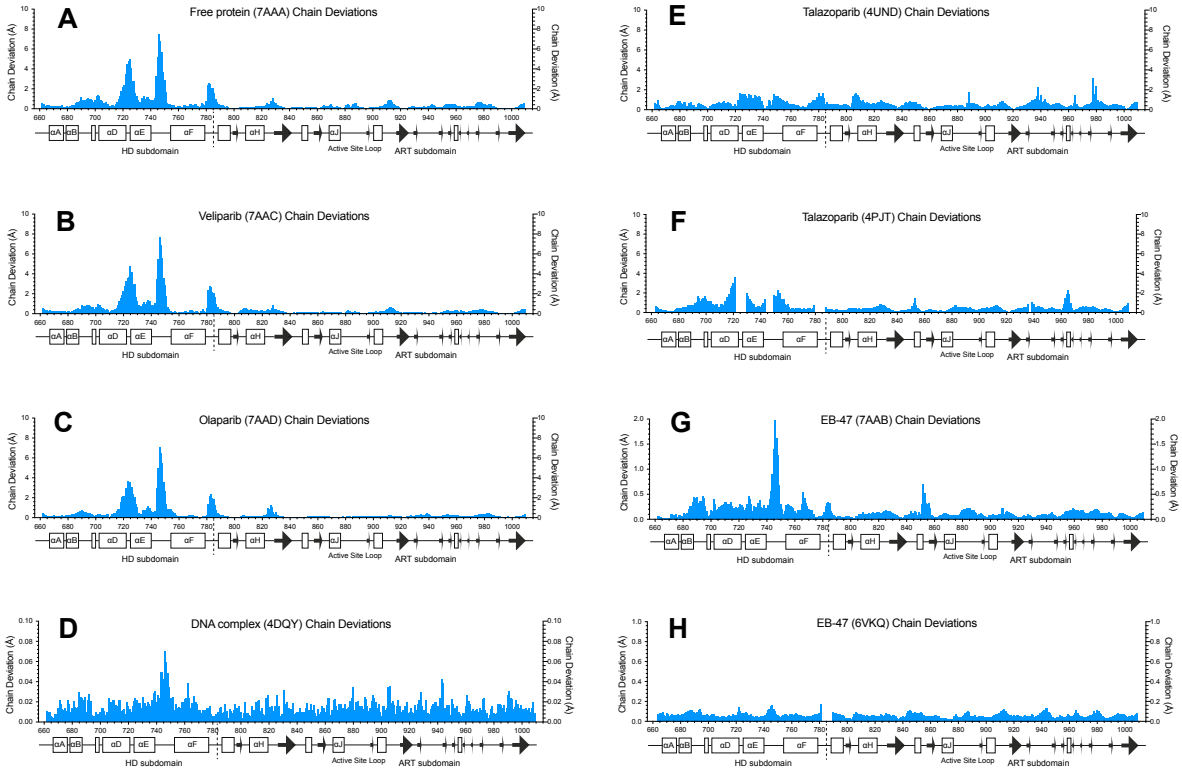

Supplementary Figure S24. Co-ordinate deviations between the different protein chains in the asymmetric unit for the structures of free PARP-1 CAT domain (7AAA, panel A) and its complexes with talazoparib (4UND and 4PJT, panels B and D), veliparib (7AAC, panel C; the other structure of veliparib, 2RD6, has only one protein chain in the asymmetric unit), olaparib (7AAD, panel E), and EB-47 (7AAB and 6BVQ, panels F and H), as well as for chains C and F of the complex of PARP-1 F1, F3 and WGR-CAT with a DNA duplex (4DQY, panel G). In each case, the values shown were calculated by first determining the best ensemble superposition of all of the protein chains in the asymmetric unit for the relevant structure using the program CLUSTERPOSE ["Co-ordinate-based cluster analysis", R. Diamond (1995), Acta Cryst D., 51, 125-135], and then calculating separately for each residue in the sequence the average deviation across all occurrences of the backbone atoms N, C^{α} and C'. Note the different vertical expansions of panels D, G and H; the relatively uniform lower values seen for structures 4UND (panel E) and 6VKQ (panel G) likely reflect the use of strongly weighted non-crystallographic symmetry terms during refinement.

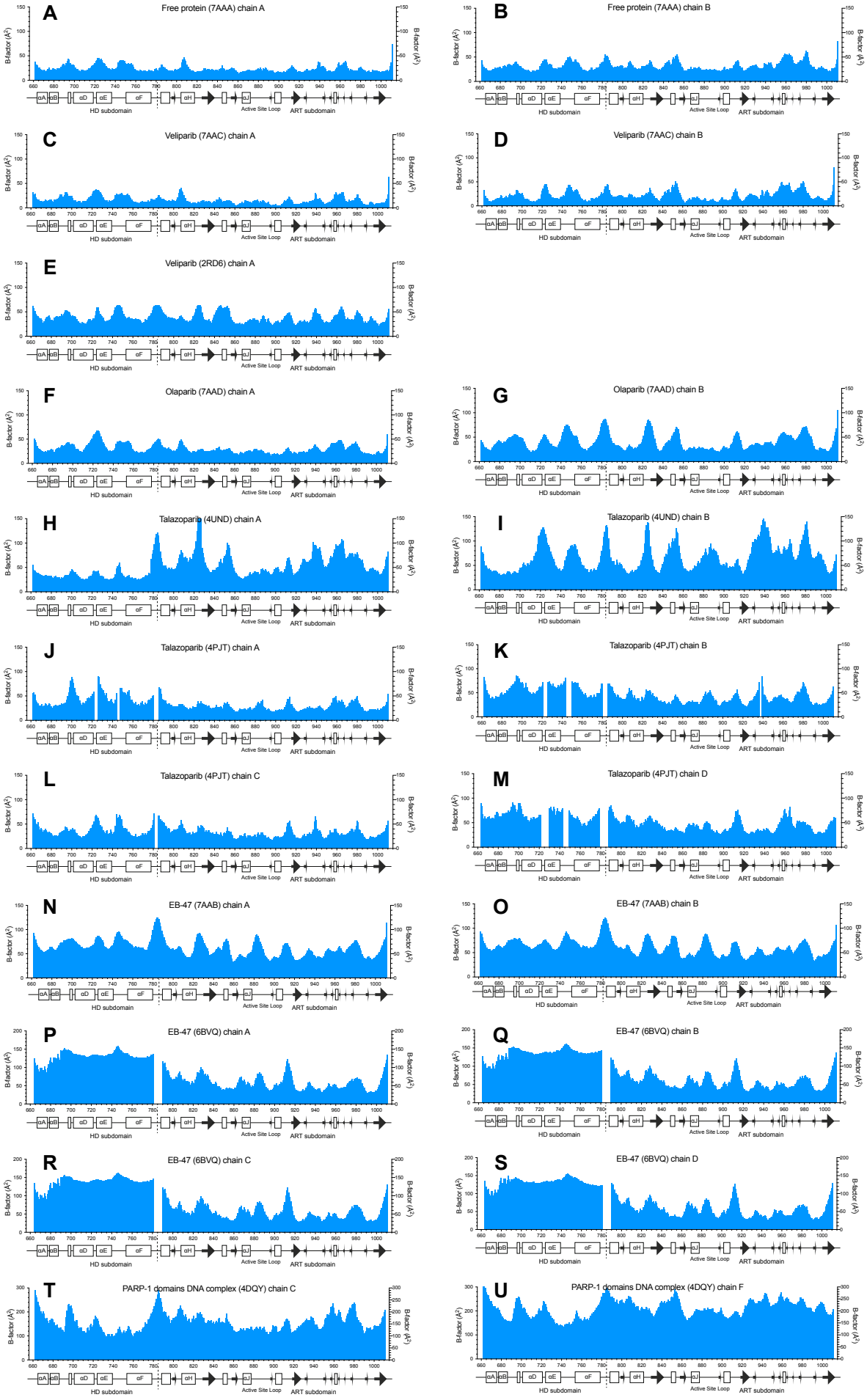
A
Free protein (7AAA) chain A
B
Free protein (7AAA) chain B
C
Veliparib (7AAC) chain A
D
Veliparib (7AAC) chain B
E
Veliparib (2RD6) chain A
F
Olaparib (7AAD) chain A
G
Olaparib (7AAD) chain B
H
Talazoparib (4UND) chain A
I
Talazoparib (4UND) chain B
J
Talazoparib (4PJT) chain A
K
Talazoparib (4PJT) chain B
L
Talazoparib (4PJT) chain C
M
Talazoparib (4PJT) chain D
N
EB-47 (7AAB) chain A
O
EB-47 (7AAB) chain B
P
EB-47 (6BVQ) chain A
Q
EB-47 (6BVQ) chain B
R
EB-47 (6BVQ) chain C
S
EB-47 (6BVQ) chain D
T
PARP-1 domains DNA complex (4DQY) chain C
U
PARP-1 domains DNA complex (4DQY) chain F
B-factor (Å²)
HD subdomain
Active Site Loop
ART subdomain

Supplementary Figure S25. B factors for each chain in each of the structures of free PARP-1 CAT domain (7AAA, panels A and B) and its complexes with veliparib (7AAC, panels C and, and 2RD6, panel E), olaparib (7AAD, panels F and G), talazoparib (4UND, panels H and I, and 4PJT, panels J - M), and EB-47 (7AAB, panels N and O, and 6BVQ, panels P - S), as well as for chains C and F of the complex of PARP-1 F1, F3 and WGR-CAT with a DNA duplex (4DQY, panels T and U). Note the different vertical scales: panels A-O run to 150 $Å^2$, panels P-S run to 200 $Å^2$, and panels T and U run to 300 $Å^2$.

Supplementary Table S1. Superposition statistics for individual helices of PARP-1 CAT domain.

Fitted onto 7AAA chain A	**Helix A**	**Helix B**	**Helix D**	**Helix E**	**Helix F**	**Helix G**	**Helix H**	**Helix I**	**Helix J**	**Helix K**
sequence	*666-677*	*679-688*	*702-722*	*725-740*	*754-779*	*788-797*	*808-821*	*848-853*	*868-876*	*900-906*
# residues	*12*	*10*	*21*	*16*	*26*	*10*	*14*	*6*	*9*	*7*
	(Å)	(Å)	(Å)	(Å)	(Å)	(Å)	(Å)	(Å)	(Å)	(Å)
2PAW A	0.129	0.106	0.359	1.050	0.453	0.227	0.165	0.667	0.143	0.211
1A26 A	0.147	0.104	0.383	1.085	0.494	0.200	0.161	0.663	0.126	0.115
4DQY C	0.235	0.561	0.477	1.024	0.834	0.401	0.348	0.566	0.267	0.222
4DQY F	0.241	0.564	0.476	1.021	0.832	0.403	0.348	0.565	0.267	0.217
7AAC A	0.047	0.038	0.122	0.101	0.117	0.054	0.069	0.045	0.044	0.052
7AAC B	0.073	0.038	0.502	1.131	0.246	0.083	0.088	0.037	0.047	0.058
2RD6	0.139	0.143	0.294	1.038	0.416	0.227	0.188	0.657	0.092	0.253
7AAD A	0.082	0.055	0.182	0.483	0.179	0.103	0.108	0.057	0.080	0.084
7AAD B	0.108	0.056	0.498	1.172	0.248	0.117	0.117	0.083	0.082	0.108
4PJT A	0.112	0.127	0.320[a]	0.198[b]	0.506	0.133	0.180	0.160	0.090	0.091
4PJT B	0.100	0.077	0.436[a]	0.231[b]	0.301	0.165	0.153	0.471	0.087	0.101
4PJT C	0.093	0.089	0.428[a]	0.194[b]	0.297	0.172	0.150	0.444	0.080	0.093
4PJT D	0.098	0.117	0.352[a]	0.288[b]	0.476	0.139	0.144	0.156	0.081	0.097
4UND A	0.151	0.110	0.334	0.980	0.315	0.188	0.164	0.533	0.111	0.232
4UND B	0.129	0.118	0.409	1.053	0.395	0.173	0.194	0.540	0.111	0.232
7AAB A	0.204	0.133	0.477	1.017	0.354	0.223	0.184	0.136	0.149	0.171
7AAB B	0.215	0.115	0.472	0.899	0.345	0.232	0.177	0.262	0.147	0.170
6VKQ A	0.237	0.259	0.989	0.818	0.548	0.215[c]	0.400	0.379	0.168	0.177
6VKQ B	0.236	0.258	0.997	0.818	0.548	0.214[c]	0.400	0.378	0.168	0.176
6VKQ C	0.237	0.262	0.994	0.817	0.550	0.215[c]	0.398	0.376	0.167	0.175
6VKQ D	0.235	0.262	0.988	0.816	0.547	0.211[c]	0.400	0.377	0.169	0.176

Fitted onto 7AAA chain B	**Helix A**	**Helix B**	**Helix D**	**Helix E**	**Helix F**	**Helix G**	**Helix H**	**Helix I**	**Helix J**	**Helix K**
sequence	*666-677*	*679-688*	*702-722*	*725-740*	*754-779*	*788-797*	*808-821*	*848-853*	*868-876*	*900-906*
# residues	*12*	*10*	*21*	*16*	*26*	*10*	*14*	*6*	*9*	*7*
	(Å)	(Å)	(Å)	(Å)	(Å)	(Å)	(Å)	(Å)	(Å)	(Å)
2PAW A	0.132	0.100	0.532	0.452	0.652	0.202	0.165	0.662	0.124	0.209
1A26 A	0.137	0.107	0.570	0.455	0.683	0.182	0.163	0.660	0.119	0.133
4DQY C	0.233	0.562	0.364	0.608	0.758	0.378	0.348	0.559	0.320	0.204
4DQY F	0.238	0.565	0.362	0.605	0.757	0.381	0.348	0.558	0.320	0.200
7AAC A	0.064	0.042	0.569	1.136	0.278	0.051	0.072	0.053	0.093	0.059
7AAC B	0.045	0.033	0.145	0.372	0.141	0.053	0.090	0.039	0.076	0.040
2RD6	0.147	0.138	0.406	0.633	0.301	0.228	0.194	0.650	0.098	0.253
7AAD A	0.105	0.055	0.590	0.748	0.354	0.095	0.107	0.053	0.094	0.098
7AAD B	0.110	0.054	0.215	0.158	0.221	0.094	0.116	0.078	0.096	0.113
4PJT A	0.092	0.127	0.492[a]	0.301[b]	0.627	0.116	0.185	0.155	0.129	0.116
4PJT B	0.090	0.079	0.209[a]	0.234[b]	0.306	0.139	0.156	0.463	0.127	0.128
4PJT C	0.085	0.092	0.287[a]	0.235[b]	0.327	0.154	0.152	0.438	0.121	0.120
4PJT D	0.089	0.117	0.459[a]	0.276[b]	0.526	0.122	0.146	0.150	0.122	0.124
4UND A	0.144	0.108	0.377	0.578	0.446	0.161	0.165	0.525	0.150	0.216
4UND B	0.127	0.113	0.317	0.563	0.343	0.147	0.197	0.533	0.137	0.217
7AAB A	0.177	0.134	0.424	0.509	0.250	0.200	0.187	0.127	0.190	0.167
7AAB B	0.189	0.119	0.416	0.537	0.223	0.207	0.180	0.255	0.189	0.166
6VKQ A	0.237	0.270	1.259	1.272	0.643	0.221[c]	0.405	0.371	0.143	0.194
6VKQ B	0.236	0.269	1.273	1.275	0.644	0.220[c]	0.406	0.370	0.144	0.193
6VKQ C	0.238	0.273	1.268	1.276	0.647	0.221[c]	0.403	0.368	0.143	0.191
6VKQ D	0.235	0.274	1.257	1.272	0.642	0.217[c]	0.406	0.369	0.143	0.192

Only helices with 6 or more residues are shown.

[a] 4PJT uses residues 702-721 for helix D

[b] 4PJT uses residues 730-740 for helix E

[c] 6VKQ uses residues 790-797 for helix G

Supplementary Table S2. Superposition statistics for groups of helices in PARP-1 HD subdomain, demonstrating differences in helical packing.

Fitted onto 7AAA chain A	Helices A and B	Helices D and E	Helices D and F	Helices E and F	Helices D, E and F
	(Å)	(Å)	(Å)	(Å)	(Å)
2PAW A	0.278	0.563	0.549	0.599	0.599
1A26 A	0.302	0.586	0.594	0.630	0.635
4DQY C	0.621	0.696	1.294	0.936	1.197
4DQY F	0.625	0.696	1.292	0.934	1.196
7AAC A	0.043	0.115	0.131	0.123	0.131
7AAC B	0.105	0.653	0.638	0.440	0.683
2RD6	0.372	0.496	0.419	0.415	0.476
7AAD A	0.093	0.200	0.226	0.204	0.222
7AAD B	0.096	0.586	0.517	0.367	0.559
4PJT A	0.460	0.367	0.867	0.619	0.802
4PJT B	0.308	0.488	0.477	0.361	0.477
4PJT C	0.307	0.466	0.496	0.333	0.471
4PJT D	0.332	0.413	0.619	0.542	0.588
4UND A	0.671	0.679	0.446	0.507	0.603
4UND B	0.605	0.649	0.482	0.453	0.572
7AAB A	0.499	0.632	0.568	0.555	0.643
7AAB B	0.433	0.674	0.572	0.549	0.658
6VKQ A	0.511	0.900	0.831	0.729	0.855
6VKQ B	0.514	0.897	0.830	0.727	0.853
6VKQ C	0.528	0.897	0.833	0.734	0.856
6VKQ D	0.538	0.895	0.831	0.732	0.854

Fitted onto 7AAA chain B	Helices A and B	Helices D and E	Helices D and F	Helices E and F	Helices D, E and F
	(Å)	(Å)	(Å)	(Å)	(Å)
2PAW A	0.289	0.593	0.862	0.753	0.850
1A26 A	0.319	0.612	0.889	0.787	0.878
4DQY C	0.614	0.629	1.414	0.873	1.296
4DQY F	0.618	0.627	1.412	0.871	1.294
7AAC A	0.127	0.652	0.621	0.441	0.660
7AAC B	0.079	0.136	0.154	0.151	0.159
2RD6	0.301	0.495	0.602	0.413	0.620
7AAD A	0.186	0.597	0.671	0.480	0.679
7AAD B	0.135	0.201	0.290	0.212	0.271
4PJT A	0.383	0.558	1.222	0.801	1.146
4PJT B	0.246	0.345	0.411	0.411	0.439
4PJT C	0.246	0.422	0.549	0.434	0.555
4PJT D	0.254	0.518	0.901	0.612	0.849
4UND A	0.607	0.632	0.678	0.682	0.776
4UND B	0.526	0.412	0.429	0.451	0.496
7AAB A	0.425	0.490	0.371	0.582	0.521
7AAB B	0.364	0.509	0.323	0.555	0.500
6VKQ A	0.450	1.036	1.032	0.873	1.048
6VKQ B	0.451	1.034	1.034	0.872	1.048
6VKQ C	0.465	1.035	1.036	0.879	1.052
6VKQ D	0.473	1.030	1.029	0.875	1.045

These fits use residues 702-721 for helix D and residues 730-740 for helix E throughout; helcies A, B and F follow the same definitions as in Table S1.

Supplementary Table S3. Superposition statistics for individual helices in PARP-1 HD subdomain, comparing different chains in the same structure.

7AAA	**Helix A**	**Helix B**	**Helix D**	**Helix E**	**Helix F**	**Helix G**	**Helix H**	**Helix I**	**Helix J**	**Helix K**
sequence	*666-677*	*679-688*	*702-722*	*725-740*	*754-779*	*788-797*	*808-821*	*848-853*	*868-876*	*900-906*
# residues	*12*	*10*	*21*	*16*	*26*	*10*	*14*	*6*	*9*	*7*
	(Å)	(Å)	(Å)	(Å)	(Å)	(Å)	(Å)	(Å)	(Å)	(Å)
A vs B	0.052	0.029	0.550	1.197	0.289	0.044	0.016	0.016	0.101	0.045

4DQY	**Helix A**	**Helix B**	**Helix D**	**Helix E**	**Helix F**	**Helix G**	**Helix H**	**Helix I**	**Helix J**	**Helix K**
sequence	*666-677*	*679-688*	*702-722*	*725-740*	*754-779*	*788-797*	*808-821*	*848-853*	*868-876*	*900-906*
# residues	*12*	*10*	*21*	*16*	*26*	*10*	*14*	*6*	*9*	*7*
	(Å)	(Å)	(Å)	(Å)	(Å)	(Å)	(Å)	(Å)	(Å)	(Å)
A vs B	0.013	0.014	0.015	0.021	0.018	0.010	0.016	0.010	0.014	0.018

7AAC	**Helix A**	**Helix B**	**Helix D**	**Helix E**	**Helix F**	**Helix G**	**Helix H**	**Helix I**	**Helix J**	**Helix K**
sequence	*666-677*	*679-688*	*702-722*	*725-740*	*754-779*	*788-797*	*808-821*	*848-853*	*868-876*	*900-906*
# residues	*12*	*10*	*21*	*16*	*26*	*10*	*14*	*6*	*9*	*7*
	(Å)	(Å)	(Å)	(Å)	(Å)	(Å)	(Å)	(Å)	(Å)	(Å)
A vs B	0.057	0.029	0.532	1.074	0.195	0.044	0.037	0.025	0.031	0.038

7AAD	**Helix A**	**Helix B**	**Helix D**	**Helix E**	**Helix F**	**Helix G**	**Helix H**	**Helix I**	**Helix J**	**Helix K**
sequence	*666-677*	*679-688*	*702-722*	*725-740*	*754-779*	*788-797*	*808-821*	*848-853*	*868-876*	*900-906*
# residues	*12*	*10*	*21*	*16*	*26*	*10*	*14*	*6*	*9*	*7*
	(Å)	(Å)	(Å)	(Å)	(Å)	(Å)	(Å)	(Å)	(Å)	(Å)
A vs B	0.060	0.022	0.532	0.720	0.224	0.045	0.020	0.043	0.013	0.053

4PJT	**Helix A**	**Helix B**	**Helix D**	**Helix E**	**Helix F**	**Helix G**	**Helix H**	**Helix I**	**Helix J**	**Helix K**
sequence	*666-677*	*679-688*	*702-721*	*730-740*	*754-779*	*788-797*	*808-821*	*848-853*	*868-876*	*900-906*
# residues	*12*	*10*	*21*	*16*	*26*	*10*	*14*	*6*	*9*	*7*
	(Å)	(Å)	(Å)	(Å)	(Å)	(Å)	(Å)	(Å)	(Å)	(Å)
A vs B	0.042	0.076	0.387	0.337	0.483	0.051	0.056	0.359	0.040	0.026
A vs C	0.044	0.101	0.303	0.092	0.395	0.064	0.066	0.332	0.036	0.040
A vs D	0.037	0.089	0.126	0.164	0.247	0.036	0.071	0.030	0.036	0.026
B vs C	0.036	0.069	0.126	0.058	0.113	0.058	0.049	0.083	0.036	0.036
B vs D	0.028	0.087	0.350	0.162	0.414	0.056	0.054	0.359	0.054	0.023
C vs D	0.029	0.051	0.260	0.161	0.328	0.061	0.036	0.335	0.038	0.027

4PJT uses residues 702-721 for helix D;
4PJT uses residues 730-740 for helix E;

4UND	**Helix A**	**Helix B**	**Helix D**	**Helix E**	**Helix F**	**Helix G**	**Helix H**	**Helix I**	**Helix J**	**Helix K**
sequence	*666-677*	*679-688*	*702-722*	*725-740*	*754-779*	*788-797*	*808-821*	*848-853*	*868-876*	*900-906*
# residues	*12*	*10*	*21*	*16*	*26*	*10*	*14*	*6*	*9*	*7*
	(Å)	(Å)	(Å)	(Å)	(Å)	(Å)	(Å)	(Å)	(Å)	(Å)
A vs B	0.056	0.086	0.305	0.245	0.368	0.046	0.100	0.019	0.058	0.036

7AAB	**Helix A**	**Helix B**	**Helix D**	**Helix E**	**Helix F**	**Helix G**	**Helix H**	**Helix I**	**Helix J**	**Helix K**
sequence	*666-677*	*679-688*	*702-722*	*725-740*	*754-779*	*788-797*	*808-821*	*848-853*	*868-876*	*900-906*
# residues	*12*	*10*	*21*	*16*	*26*	*10*	*14*	*6*	*9*	*7*
	(Å)	(Å)	(Å)	(Å)	(Å)	(Å)	(Å)	(Å)	(Å)	(Å)
A vs B	0.058	0.033	0.110	0.186	0.137	0.019	0.013	0.270	0.044	0.010

Supplementary Table S3 (continued). Superposition statistics for individual helices in PARP-1 HD subdomain, comparing different chains in the same structure.

6VKQ	**Helix A**	**Helix B**	**Helix D**	**Helix E**	**Helix F**	**Helix G**	**Helix H**	**Helix I**	**Helix J**	**Helix K**
sequence	*666-677*	*679-688*	*702-722*	*725-740*	*754-779*	*790-797*	*808-821*	*848-853*	*868-876*	*900-906*
# residues	*12*	*10*	*21*	*16*	*26*	*10*	*14*	*6*	*9*	*7*
	(Å)	(Å)	(Å)	(Å)	(Å)	(Å)	(Å)	(Å)	(Å)	(Å)
A vs B	0.007	0.006	0.025	0.006	0.010	0.005	0.009	0.005	0.005	0.003
A vs C	0.008	0.012	0.018	0.007	0.013	0.004	0.013	0.011	0.003	0.008
A vs D	0.010	0.016	0.011	0.008	0.015	0.009	0.012	0.005	0.007	0.008
B vs C	0.011	0.011	0.012	0.008	0.015	0.007	0.012	0.008	0.005	0.007
B vs D	0.011	0.014	0.022	0.009	0.018	0.011	0.013	0.007	0.008	0.006
C vs D	0.005	0.006	0.015	0.009	0.009	0.010	0.007	0.009	0.007	0.004

6VKQ uses residues 790-797 for helix G.

Supplementary Table S4. Superposition statistics for the HD and ART subdomains of PARP-1 CAT domain (all chains onto 7AAA).

Fitted atoms (set 1)	Resolution	Space group	CAT	ART	HD	ART	HD
Measured atoms (set 2)			CAT	ART	HD	HD	ART
(all fitted onto 7AAA chain A)	(Å)		(Å)	(Å)	(Å)	(Å)	(Å)
2PAW A (apo-protein)	2.30	$P\ 2_12_12_1$	0.679	0.568	0.630	1.041	0.976
1A26 A (apo-protein)	2.25	$P\ 2_12_12_1$	0.681	0.496	0.646	1.189	1.033
4DQY C (apo-protein)	3.25	$P\ 2_12_12_1$	1.293	0.804	1.566	2.233	2.328
4DQY F (apo-protein)	"	"	1.294	0.806	1.565	2.234	2.340
7AAC A (veliparib complex)	1.59	$P\ 2_12_12_1$	0.145	0.133	0.120	0.181	0.389
7AAC B (veliparib complex)	"	"	0.494	0.222	0.697	0.952	0.885
2RD6 A (veliparib complex)	2.30	P 3 2 1	0.980	0.855	0.541	1.720	1.550
7AAD A (olaparib complex)	2.21	$P\ 2_12_12_1$	0.247	0.237	0.224	0.278	0.463
7AAD B (olaparib complex)	"	"	0.446	0.303	0.609	0.682	0.649
4UND A (talazoparib complex)	2.20	$P\ 2_12_12_1$	1.174	0.760	0.850	2.429	2.855
4UND B (talazoparib complex)	"	"	1.152	0.855	0.823	2.140	2.877
4PJT A (talazoparib complex)	2.35	$P\ 2_12_12_1$	1.185	0.690	0.847	2.574	3.042
4PJT B (talazoparib complex)	"	"	0.932	0.667	0.546	1.942	1.575
4PJT C (talazoparib complex)	"	"	0.952	0.716	0.528	1.930	1.783
4PJT D (talazoparib complex)	"	"	1.044	0.664	0.653	2.311	2.177
7AAB A (EB-47 complex)	2.8	$P\ 6_1$	1.791	0.506	0.972	4.178	4.352
7AAB B (EB-47 complex)	"	"	1.822	0.506	0.985	4.193	4.750
6VKQ A (EB-47 complex)	2.9	$P\ 4_12_12$	1.421	0.771	0.997	3.166	2.763
6VKQ B (EB-47 complex)	"	"	1.421	0.770	0.990	3.171	2.782
6VKQ C (EB-47 complex)	"	"	1.432	0.780	1.003	3.181	2.829
6VKQ D (EB-47 complex)	"	"	1.448	0.780	1.003	3.217	2.870

Fitted atoms (set 1)	Resolution	Space group	CAT	ART	HD	ART	HD
Measured atoms (set 2)			CAT	ART	HD	HD	ART
(all fitted onto 7AAA chain B)	(Å)		(Å)	(Å)	(Å)	(Å)	(Å)
2PAW A (apo-protein)	2.30	$P\ 2_12_12_1$	0.848	0.599	0.962	1.431	1.543
1A26 A (apo-protein)	2.25	$P\ 2_12_12_1$	0.855	0.530	0.960	1.581	1.683
4DQY C (apo-protein)	3.25	$P\ 2_12_12_1$	1.465	0.854	1.741	2.584	3.368
4DQY F (apo-protein)	"	"	1.466	0.855	1.741	2.585	3.380
7AAC A (veliparib complex)	1.59	$P\ 2_12_12_1$	0.529	0.199	0.710	1.021	1.459
7AAC B (veliparib complex)	"	"	0.189	0.180	0.154	0.228	0.346
2RD6 A (veliparib complex)	2.30	P 3 2 1	1.034	0.863	0.635	1.770	2.238
7AAD A (olaparib complex)	2.21	$P\ 2_12_12_1$	0.585	0.287	0.755	1.100	1.506
7AAD B (olaparib complex)	"	"	0.364	0.329	0.285	0.581	0.667
4UND A (talazoparib complex)	2.20	$P\ 2_12_12_1$	1.298	0.745	0.913	2.789	3.841
4UND B (talazoparib complex)	"	"	1.193	0.842	0.658	2.210	3.863
4PJT A (talazoparib complex)	2.35	$P\ 2_12_12_1$	1.366	0.702	1.165	2.868	4.070
4PJT B (talazoparib complex)	"	"	1.029	0.675	0.627	2.227	2.253
4PJT C (talazoparib complex)	"	"	1.055	0.727	0.606	2.194	2.614
4PJT D (talazoparib complex)	"	"	1.146	0.680	0.845	2.400	3.077
7AAB A (EB-47 complex)	2.8	$P\ 6_1$	1.803	0.551	0.911	4.267	4.089
7AAB B (EB-47 complex)	"	"	1.818	0.550	0.920	4.239	4.364
6VKQ A (EB-47 complex)	2.9	$P\ 4_12_12$	1.538	0.778	1.192	3.425	3.445
6VKQ B (EB-47 complex)	"	"	1.540	0.778	1.185	3.437	3.479
6VKQ C (EB-47 complex)	"	"	1.550	0.787	1.198	3.440	3.542
6VKQ D (EB-47 complex)	"	"	1.562	0.786	1.194	3.466	3.569

The atoms used for superposition were as follows:
HD = 666-721, 730-743, 750-779 (N,C^{α},C');
ART = 790-936, 939-1009 (N,C^{α},C');
Set 1 atoms are used to calculate transformed co-ordinates resulting from fitting;
Set 2 atoms are used to calculate an rms difference without further changing the co-ordinates.

Supplementary Table S5. Superposition statistics for the HD and ART subdomains of PARP-1 CAT domain between different complexes with the same inhibitor (all chains).

Fitted atoms (set 1)	**CAT**	**ART**	**HD**	**ART**	**HD**
Measured atoms (set 2)	**CAT**	**ART**	**HD**	**HD**	**ART**
	(Å)	(Å)	(Å)	(Å)	(Å)
Comparing veliparib complexes					
7AAC A vs 2RD6 A	0.983	0.874	0.518	1.710	1.442
7AAC B vs 2RD6 A	1.040	0.869	0.648	1.758	2.091
Comparing talazoparib complexes					
4PJT A vs 4UND A	0.955	0.712	0.867	1.640	1.429
4PJT A vs 4UND B	0.653	0.542	0.612	0.908	1.957
4PJT A vs 4UND C	0.653	0.574	0.588	0.921	1.495
4PJT A vs 4UND D	0.961	0.680	0.782	1.855	1.616
4PJT B vs 4UND A	0.822	0.695	0.944	1.174	0.867
4PJT B vs 4UND B	0.787	0.620	0.584	1.310	2.204
4PJT B vs 4UND C	0.685	0.608	0.531	1.016	1.641
4PJT B vs 4UND D	0.725	0.671	0.699	0.913	1.184
Comparing EB-47 complexes					
7AAB A vs 6VKQ A	1.083	0.642	0.884	1.835	3.822
7AAB A vs 6VKQ B	1.092	0.641	0.884	1.856	3.880
7AAB A vs 6VKQ C	1.100	0.646	0.895	1.863	3.994
7AAB A vs 6VKQ D	1.084	0.648	0.888	1.822	3.925
7AAB B vs 6VKQ A	1.159	0.644	0.925	1.976	4.458
7AAB B vs 6VKQ B	1.170	0.644	0.926	2.000	4.516
7AAB B vs 6VKQ C	1.178	0.648	0.939	2.007	4.613
7AAB B vs 6VKQ D	1.161	0.650	0.932	1.964	4.536

The atoms used for superposition were as follows:
HD = 666-721, 730-743, 750-779 (N,C^{α},C');
ART = 790-936, 939-1009 (N,C^{α},C');
Set 1 atoms are used to calculate transformed co-ordinates resulting from fitting;
Set 2 atoms are used to calculate an rms difference without further changing the co-ordinates.

Supplementary Table S6. Binding affinities and dissociation rate constants for PARP inhibitors as determined in this work and in the literature.

Inhibitor	Technique	PARP	DNA	veliparib	olaparib	talazoparib	EB-47
K_D (M) [a]	SPR	FL	none	3.82 ± 0.35 E-09	5.90 ± 1.60 E-10	4.94 ± 0.67 E-10	6.46 ± 1.31 E-07
K_D (M) [b]	SPR	FL	none	4.4 E-09	1.3 E-09	1.7 E-10	-
K_D (M) [b]	TR-FRET	FL	none	2.0 ± 0.2 E-09	8.6 ± 2.6 E-10	4.7 ± 1.1 E-10	-
K_D (M) [b]	TR-FRET	FL	SSB	3.3 ± 2.3 E-09	1.3 ± 0.7 E-09	5.0 ± 2.6 E-10	-
K_D (M) [c]	SPR	CAT	none	1.7 ± 0.3 E-09	2.4 ± 1.2 E-10	-	-
K_D (M) [c]	FP	FL	none	<3 E-08	<3 E-08	-	1.5 ± 0.2 E-07
k_D (s^{-1}) [a]	SPR	FL	none	4.60 ± 1.60 E-03	1.48 ± 0.35 E-04	1.05 ± 0.28 E-04	1.60 ± 0.50 E-01
k_D (s^{-1}) [b]	SPR	FL	none	7.0 E-03	3.2 E-04	6.3 E-05	-

[a] This work

[b] T.A. Hopkins *et al*. (2015) *Molecular Cancer Research*, **33**, 1465-1477.

[c] G. Papeo *et al*. (2014) *J. Biomol. Screen.*, **19**, 1212-1219.